

# A Numerical Study of Near Inertial Motions in Mid-Atlantic Bight Area Induced by Hurricane Irene (2011)

Peida Han<sup>1</sup> and Xiping Yu<sup>2</sup>

## Abstract

Hurricane Irene generated strong near inertial currents (NICs) in the ocean waters when passing over the Mid-Atlantic Bight (MAB) of the U. S. East Coast in late August 2011. It is demonstrated that a combination of the valuable field data with detailed model results can be taken advantage to study the development and decay mechanism of this event. Numerical results obtained with regional oceanic modeling system (ROMS) are shown to agree well with the field data. Both computed and observed results show that the NICs were significant in most areas of the MAB region except in the nearshore area where the stratification was totally destroyed by the hurricane-induced strong mixing. Based on the energy budget, it is clarified that the near inertial kinetic energy (NIKE) was mainly gained from the wind power during the hurricane event. In the deep water region, NIKE was basically balanced by the vertical turbulence diffusion (40%) and downward divergence (33%). While in the continental shelf region, NIKE was mainly dissipated by the vertical turbulence diffusion (67%) and partially by the bottom friction (24%). Local dissipation of NIKE due to turbulence diffusion is much more closely related to the rate of the vertical shear rather than the intensity of turbulence. The strong vertical shear at the offshore side of the continental shelf led to a rapid dissipation of NIKE in this region.

**Keywords:** Hurricane Irene (2011); Mid-Atlantic Bight; Near inertial current; Energy budget; Timescale of near inertial energy decay

**Correspondence to:** Xiping Yu (yuxp@sustech.edu.cn)

---

<sup>1</sup> PhD Candidate. Department of Hydraulic Engineering, Tsinghua University, Beijing, China.

<sup>2</sup> Professor. Department of Ocean Science and Engineering, Southern University of Science and Technology, Shenzhen, China.

## 24 **1. Introduction**

25 Near inertial currents (NICs), observed widely in ocean basins around the world, are  
26 characterized by the important role of Coriolis effect and by the periodic motion with the  
27 frequency of an inertial mode (Garrett, 2001). The basic energy source of these freely  
28 flowing currents is the wind power (Pollard, 1980; D'Asaro et al., 1985). Globally, the  
29 annually averaged wind power supply to NICs was estimated ranging from 0.3 TW to more  
30 than 1 TW by previous investigators (Alford, 2003a; Furuichi et al., 2008; Rimac et al.,  
31 2013). As a comparison, the total power required to maintain the abyssal stratification and  
32 the thermohaline circulation is about 2 TW (Munk and Wunsch, 1998). This implies that  
33 NIC is a very important phenomenon in physical oceanography (Gregg, 1987; Alford, 2003b;  
34 Jochum et al., 2013).

35 A tropical or an extratropical cyclone (hereinafter collectively referred as TC) is a  
36 rotating low-pressure and strong-wind mesoscale weather system, which generates NICs  
37 more powerfully than other types of atmospheric processes in nature (Alford et al., 2016;  
38 Steiner et al., 2017). When a TC passes over a deep ocean, enormous energy is directly  
39 transferred into the ocean waters, which rapidly generates strong NICs with a velocity up to  
40 1 m/s in the horizontal direction of the mixed layer (Price, 1983; Sanford et al., 2011). Right-  
41 bias effect is often shown in the NIC pattern, i.e., NICs are more intense on the right side of  
42 the hurricane track, due to the resonance between the surface flow driven by NICs and  
43 clockwise rotating wind stress on the right side (Chang and Anthes, 1978; Price, 1994).  
44 After the passage of a TC, the surface near inertial energy usually persists for several inertial  
45 cycles, and then gradually decays (Price, 1983; Sanford et al., 2011; Hormann et al., 2014;  
46 Zhang et al., 2016; Wu et al., 2020).

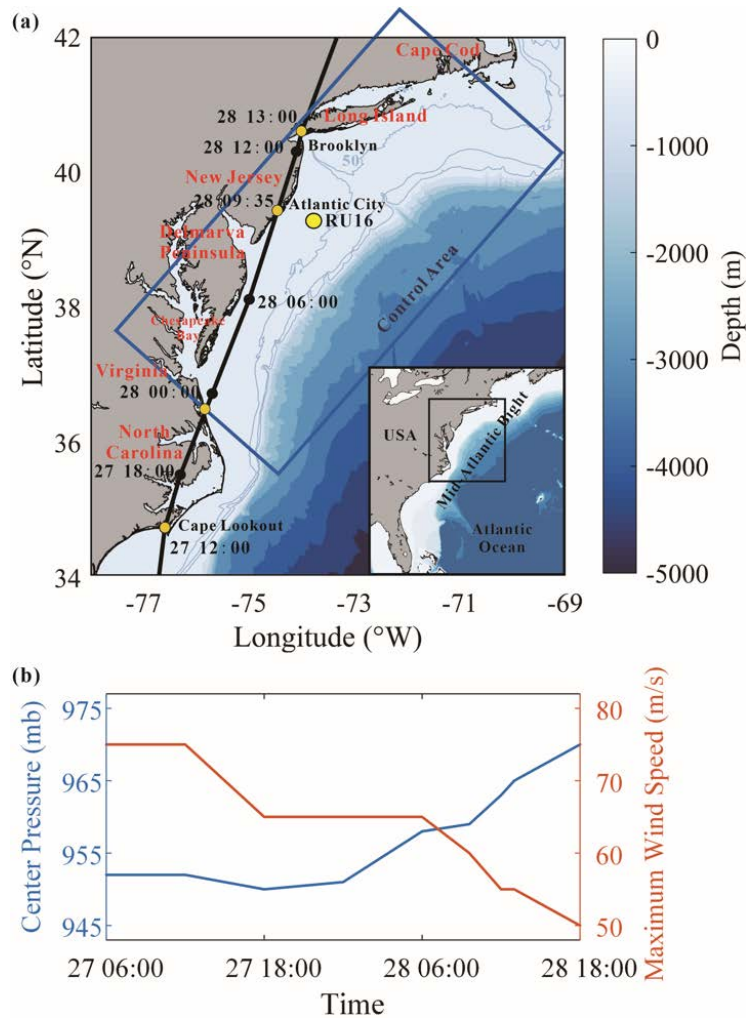
47 It is known that NICs in shallow waters show some significant differences with those  
48 in deep waters and the velocity of NICs in shallow waters is usually of a smaller magnitude  
49 of 0.1-0.5 m/s (Chen and Xie, 1997; Rayson et al., 2015; Yang et al., 2015; Chen et al., 2017;  
50 Zhang et al., 2018). The decrease of current velocity in shallow waters may be an effect of  
51 the sea-bottom friction as Rayson et al. (2015) pointed out. Chen and Xie (1997), however,

52 found that it was because a significant part of the wind input, which may otherwise be an  
53 energy source of the NICs, was exhausted to generate a wave-induced nearshore current  
54 system. Chen et al. (2017) considered that barotropic waves in the shallow waters, such as  
55 seiches, may trap some wind energy. In addition to the difference in magnitude, the modes  
56 of the NICs in shallow and deep waters are also different. More specifically, a two-layer  
57 structure was observed in shallow waters in several studies, i.e., NICs were in opposite  
58 phases in surface and bottom layers, which differed from the conventional multi-layer mode  
59 in deep waters (Chen et al., 1996; Shearman, 2005; Yang et al., 2015), though a multi-layer  
60 mode may also be observed sometimes in nearshore waters due to combined effect of  
61 changing wind stress, variable stratification and nonlinear bottom friction (Mackinnon and  
62 Gregg, 2005).

63 There have been a considerable number of studies on the decay of specific TC  
64 generated NICs in coastal regions. Rayson et al. (2015) paid attention to four intense TCs  
65 on the Australian North-West Shelf and related the rapid decay of NICs in shallow waters  
66 to the bottom friction. Yang et al. (2015) examined coastal ocean responses to Typhoon  
67 Washi and found that the negative background vorticity could trap near inertial energy and  
68 result in a slow decay. Shen et al. (2017) investigated five TCs over the Taiwan Strait and  
69 identified a rapid decaying rate due to nonlinear interaction between NICs and tides. Zhang  
70 et al. (2018) studied Hurricane Arthur in Mid-Atlantic Bight and showed that excessive wind  
71 input does not necessarily lead to amplification of NICs because intensive wind input is  
72 usually accompanied by an even higher rate of energy dissipation.

73 Though a significant number of investigations have been conducted, some basic  
74 features of a TC induced NIC in the coastal ocean are still not clarified. For instance, the  
75 energy budget in the NIC generated by a TC has not yet been thoroughly discussed in either  
76 deep or shallow waters; and the relative importance of different physical processes including  
77 advection, conversion, turbulence diffusion, bottom friction, energy divergence, etc., in the  
78 energy budget has not yet been fully understood. In addition, it is still not concluded on  
79 which processes dominate the decay of near inertial energy or on how each physical process

80 affects the decay rate of the near inertial energy in deep and shallow waters, respectively.  
 81 Our limited understanding to the basic features of a TC induced NIC is largely due to the  
 82 difficulties in ocean observations under extreme weather.  
 83



84  
 85 Figure 1. (a) Map of the MAB region. Best track of Hurricane Irene (2011) reported by Avila  
 86 and Cangialosi (2011) is shown by a black line. Reanalysis data provided by H\*WIND  
 87 shows a similar track with Avila and Cangialosi (2011) and is thus omitted. The mean  
 88 position of Glider RU16 is marked by a yellow circle. The control domain defined in Section  
 89 4 is marked by a blue box. (b) Time series of center pressure and 10-m maximum wind  
 90 speed of Hurricane Irene reported by Avila and Cangialosi (2011).  
 91

92 In this study, we pay a close attention to the NIC induced by Hurricane Irene (2011).  
 93 Hurricane Irene (2011) crossed over the Mid-Atlantic Bight (MAB), a coastal region of the  
 94 North Atlantic, extending from Cape Cod, Massachusetts to Cape Lookout, North Carolina,

95 USA, as shown in Figure 1a. Before the hurricane event, seawater stratification in MAB  
 96 was quite strong due to the Cold Pool effect (Lentz, 2017) and the temperature difference  
 97 between the surface and the bottom exceeded 10 °C. The vertical gradient of the temperature  
 98 should also be very large because previous studies showed that the thermocline in shelf  
 99 region was rather thin; for instance, the thermocline was less than 5 m in the place where  
 100 water depth was around 40 m (Glenn et al., 2016; Seroka et al., 2017). During the passage  
 101 of Hurricane Irene (2011), a network of High-frequency (HF) radars measured the surface  
 102 currents in MAB (Roarty et al., 2010). Meanwhile, a Slocum glider launched near New  
 103 Jersey measured the vertical profiles of the temperature and the salinity (Schofield et al.,  
 104 2010). Combination of the valuable field data with effective numerical techniques then  
 105 provided an opportunity to achieve a comprehensive study of the NICs generated by this  
 106 hurricane event.

## 107 **2. Numerical Model**

### 108 **2.1 Basic Equations**

109 In this study, the ocean responses to Hurricane Irene (2011) are studied using the  
 110 regional oceanic modeling system (ROMS) (Shchepetkin and McWilliams, 2005;  
 111 Haidvogel et al., 2008). ROMS deals with the Reynolds-averaged N-S equations in the  $\sigma$   
 112 coordinate system (Freeman et al., 1972). Specifically, the Cartesian coordinate  $z$  is  
 113 replaced by  $\sigma$  based on a general relation  $\chi(\sigma) = (z - \eta) / D$ , where  $\eta$  is the vertical  
 114 displacement of the free surface and  $D$  is the instantaneous water depth, while  $\chi(\sigma)$  is  
 115 a stretching function introduced for grid refinement. In the  $\sigma$ -coordinate system the  
 116 Reynolds-averaged N-S equations may finally be expressed as

$$117 \quad \frac{\partial \xi}{\partial t} + \frac{\partial(\xi u)}{\partial x} + \frac{\partial(\xi v)}{\partial y} + \frac{\partial(\xi \omega)}{\partial \sigma} = 0 \quad (1)$$

$$\begin{aligned}
118 \quad & \frac{\partial(\xi u)}{\partial t} + \frac{\partial(\xi uu)}{\partial x} + \frac{\partial(\xi uv)}{\partial y} + \frac{\partial(\xi u\omega)}{\partial \sigma} - f\xi v + \frac{\xi}{\rho} \frac{\partial p}{\partial x} \\
& = -g\xi \left( \chi \frac{\partial D}{\partial x} + \frac{\partial \eta}{\partial x} \right) + \frac{\partial}{\partial \sigma} \left( \frac{\nu}{\xi} \frac{\partial u}{\partial \sigma} \right) + \frac{\partial}{\partial x} \left( \xi \nu' \frac{\partial u}{\partial x} \right) + \frac{\partial}{\partial y} \left( \xi \nu' \frac{\partial u}{\partial y} \right)
\end{aligned} \tag{2}$$

$$\begin{aligned}
119 \quad & \frac{\partial(\xi v)}{\partial t} + \frac{\partial(\xi uv)}{\partial x} + \frac{\partial(\xi vv)}{\partial y} + \frac{\partial(\xi v\omega)}{\partial \sigma} + f\xi u + \frac{\xi}{\rho} \frac{\partial p}{\partial y} \\
& = -g\xi \left( \chi \frac{\partial D}{\partial y} + \frac{\partial \eta}{\partial y} \right) + \frac{\partial}{\partial \sigma} \left( \frac{\nu}{\xi} \frac{\partial v}{\partial \sigma} \right) + \frac{\partial}{\partial x} \left( \xi \nu' \frac{\partial v}{\partial x} \right) + \frac{\partial}{\partial y} \left( \xi \nu' \frac{\partial v}{\partial y} \right)
\end{aligned} \tag{3}$$

$$120 \quad 0 = -\frac{1}{\rho} \frac{\partial p}{\partial \sigma} - g\xi \tag{4}$$

$$\begin{aligned}
121 \quad & \frac{\partial(\xi C)}{\partial t} + \frac{\partial(\xi uC)}{\partial x} + \frac{\partial(\xi vC)}{\partial y} + \frac{\partial(\xi \omega C)}{\partial \sigma} \\
& = \frac{\partial}{\partial \sigma} \left( \frac{\kappa}{\xi} \frac{\partial C}{\partial \sigma} \right) + \frac{\partial}{\partial x} \left( \xi \kappa' \frac{\partial C}{\partial x} \right) + \frac{\partial}{\partial y} \left( \xi \kappa' \frac{\partial C}{\partial y} \right)
\end{aligned} \tag{5}$$

122 where,  $\xi = \partial z / \partial \sigma = D(\partial \chi / \partial \sigma)$ ;  $u$ ,  $v$ ,  $\omega$  are the velocity components in  $x$ ,  $y$ ,  $\sigma$   
123 directions, respectively;  $C$  stands for the potential temperature  $T$  or salinity  $S$ ;  $p$  is  
124 the seawater pressure;  $\rho$  is the density of the seawater;  $f = 2\Omega \sin \phi$  is the Coriolis  
125 parameter with  $2\Omega = 1.458 \times 10^{-4} \text{ s}^{-1}$  and  $\phi$  being the latitude;  $\nu$  and  $\kappa$  are the  
126 diffusion coefficients for momentum and potential temperature or salinity, respectively, in  
127 the vertical direction;  $\nu'$  and  $\kappa'$  are those in the horizontal directions; Note that Eq. (1)  
128 is the continuity equation; Eqs. (2) and (3) are equations of motion in two horizontal  
129 directions; Eq. (4) is the hydrostatic assumption; Eq. (5) is the advection-diffusion equation  
130 of the potential temperature or the salinity. The density of the seawater  $\rho$  is determined  
131 following the equation of state proposed by Jackett and McDougall (1995):

$$132 \quad \rho(S, T, p) = \frac{\rho_0}{1 - p/K(S, T, p)} \tag{6}$$

133 where  $\rho_0 = \rho(S, T, 0)$  is the seawater density at the standard atmospheric pressure and  
134  $K(S, T, p)$  is the bulk modulus, both are given by Jackett and McDougall (1995).

135 The vertical mixing is known to play an important role in determining the structure of  
136 a NIC, so it must be properly evaluated. In this study, we consider  $\nu = \nu_0 + \nu_e$  and

137  $\kappa = \kappa_0 + \kappa_e$ , in which  $\nu_0$  and  $\kappa_0$  are the molecular viscosity and diffusivity of the  
138 seawater, set to  $\nu_0 = 10^{-5} \text{ m}^2/\text{s}$  and  $\kappa_0 = 10^{-6} \text{ m}^2/\text{s}$  following previous suggestions (Xu  
139 et al., 2002; Li and Zhong, 2007; Lentz, 2017), while  $\nu_e$  and  $\kappa_e$  are the eddy viscosity  
140 and diffusivity, determined by the conventional k- $\epsilon$  turbulence model (see Rodi (1987) and  
141 Umlauf and Burchard (2003) for detailed description), a widely employed model that  
142 demonstrated good performance in simulating various oceanographic processes  
143 (Olabarrieta et al., 2011; Toffoli et al., 2012; Zhang et al., 2018).

144 Horizontal mixing is included in Eqs. (2), (3) and (5), though it has been pointed out  
145 to play a relatively insignificant role in simulating response of the stratified ocean to a  
146 hurricane, as compared to vertical mixing (Li and Zhong, 2007; Zhai et al., 2009; Dorostkar  
147 et al., 2010). In the ocean basin of the present interest, the horizontal diffusion coefficient  
148 was estimated to be an order of  $10 \text{ m}^2/\text{s}$  under extreme conditions, e.g., TC condition  
149 (Allahdadi, 2014; Mulligan and Hanson, 2016). Thus, we take  $\nu' = \kappa' = 10 \text{ m}^2/\text{s}$  in the  
150 present study for simplicity to simulate the ocean response to Hurricane Irene.

## 151 2.2 Computational Conditions

152 In order to fully capture the NIC induced by Hurricane Irene (2011), our computational  
153 domain covers the entire MAB regions of the U. S. East Coast extending from Cape Cod,  
154 Massachusetts, to Cape Lookout, North Caroline. The computational domain is discretized  
155 into 35 layers with refinement near the surface and covered with a  $5 \text{ km} \times 5 \text{ km}$  grid in the  
156 horizontal plane. The 1 arc-min bathymetry data is obtained from ETOPO1 Global Relief  
157 Model (Amante and Eakins, 2009) and resampled to a resolution of 5 km. The simulation  
158 starts from 20 August, one week before the hurricane event and lasted for a period of 16  
159 days. The time step is set to 1 min.

160 The initial and open boundary conditions of the seawater temperature and salinity, the  
161 ocean flow velocities and the sea surface elevation are all from the Hybrid Coordinate Ocean  
162 Model (HYCOM, <https://www.hycom.org/>) with a resolution of  $1/12^\circ$  in space and 3 hr in  
163 time (Cummings, 2005; Chassignet et al., 2007). The initial stratification in the HYCOM is  
164 examined through a comparison with the 4D data provided by Experimental System for

165 Predicting Shelf and Slope Optics (ESPreSSO, <http://www.myroms.org/espresso/>). Seven  
 166 tidal constituents (M2, S2, N2, K2, O1, K1, Q1) included in the simulation are derived from  
 167 the ADvanced CIRCulation model (ADCIRC, <https://adcirc.org/>). Daily inflows from the  
 168 eleven largest rivers, containing Susquehanna River, Delaware River, Hudson River,  
 169 Potomac River, etc., are obtained from the United States Geological Survey (USGS,  
 170 <https://waterdata.usgs.gov/>). The so-called radiation-nudging condition is adopted at the  
 171 open boundaries (Marchesiello et al., 2001). Wet-and-dry option is activated at coastal  
 172 boundaries (Warner et al., 2013). The seabed boundary condition is required to satisfy:

$$173 \quad \nu \frac{\partial \mathbf{u}}{\partial z} = \boldsymbol{\tau}_b = \rho \left[ \frac{\lambda}{\ln(\Delta z / z_0)} \right]^2 |\mathbf{u}_b| \mathbf{u}_b \quad (7)$$

174 where,  $\boldsymbol{\tau}_b$  is the bottom friction;  $\lambda$  is the von Karman constant;  $\mathbf{u}_b$  is the fluid velocity  
 175 at the center of the bottom layer;  $\Delta z$  is the distance between the center of the bottom layer  
 176 and the seabed;  $z_0$  is the bottom roughness, which is set to 0.02 m in MAB following  
 177 Churchill et al. (1994).

178 The hurricane wind forcing required in this study can be obtained from two sources,  
 179 i.e., the H\*WIND data, with a spatial resolution of 6 km and a temporal resolution of 6 hr,  
 180 published by Atlantic Oceanographic and Meteorological Laboratory, National Oceanic and  
 181 Atmospheric Administration (AOML/NOAA) ([https://www.aoml.noaa.gov/hrd/data\\_sub/wind.html](https://www.aoml.noaa.gov/hrd/data_sub/wind.html)) (Powell et al., 1998) and the North American Mesoscale (NAM) data, with a  
 182 spatial resolution of 12 km and a temporal resolution of 3 hr, provided by National Centers  
 183 for Environmental Prediction (NCEP) (<https://www.ncdc.noaa.gov/data-access/model-data/model-datasets/north-american-mesoscale-forecast-system-nam>) (Janjic et al., 2004).  
 184 In our computation, the former is used between 26 and 31 August (during the hurricane  
 185 event) because it has a better accuracy in capturing the maximum wind speed, while the  
 186 latter is used during other periods of the simulation. Reanalysis data for other atmospheric  
 187 forcing, such as the surface air temperature, air pressure, relative humidity, radiation and  
 188 precipitation are also available from NAM for determining the surface buoyancy fluxes.  
 189  
 190

191 In this study, the boundary layer effect on the near inertial current is not directly



192 considered. The driving effect of the airflow on the near inertial current is reflected by  
 193 adding a wind drag on the ocean surface. The wind drag  $\tau_s$ , which is measure of the vertical  
 194 flux of horizontal momentum, can be estimated through (Fairall et al., 1996):

$$195 \quad \tau_s = \rho_a C_d u_{10}^2 \quad (8)$$

196 where,  $\rho_a$  is the density of the air;  $C_d$  is the drag coefficient;  $u_{10}$  is the horizontal wind  
 197 speed at the 10-m level. Traditionally, the drag coefficient  $C_d$  is expressed as a linear  
 198 function of the wind speed. In this study, we adopt a more advanced formula that fits the  
 199 numerical results obtained with an improved wave boundary layer model under extreme  
 200 wind conditions (Chen and Yu, 2016; Chen et al., 2018; Xu and Yu, 2021):

$$201 \quad C_d = C_{dw} + \frac{C_{d0} - C_{dw}}{(W_0 - W)^2} (u_{10} - W)^2 \quad (9)$$

202 where  $C_{d0}$  is a threshold value set to 0.001 for the wind stress at  $u_{10} \leq W_0 = 5$  m/s,  $C_{dw}$   
 203 is the saturated wind stress coefficient and  $W$  is the saturation wind speed. We have

$$204 \quad C_{dw} = \begin{cases} -1.86 \times 10^{-4} \ln \frac{gD}{W_D} + 0.0025 & \frac{gD}{W_D} \leq 3 \\ 0.00225 & \frac{gD}{W_D} > 3 \end{cases} \quad (10)$$

$$205 \quad W = \begin{cases} 4.64 \ln(\frac{gD}{W_D}) + 42.6 & \frac{gD}{W_D} \leq 0.6 \\ W_D & \frac{gD}{W_D} > 0.6 \end{cases} \quad (11)$$

206 where  $W_D$  set to 40 m/s is the saturation wind speed in deep water. Except for the  
 207 momentum flux, other air-sea fluxes, e.g., the sensible heat flux and the latent heat flux, are  
 208 determined based on the conventional bulk parameterization scheme (see Fairall et al. (1996)  
 209 for detailed description). The sea surface boundary condition is then required to satisfy:

$$210 \quad \nu \frac{\partial \mathbf{u}}{\partial z} = \tau_s \quad (12)$$

## 211 2.3 Observational data

212 During the passage of Hurricane Irene (2011), a network of High-frequency (HF)

213 radars measured the surface currents and a Slocum glider launched near New Jersey  
214 measured the vertical profiles of the temperature and the salinity (Roarty et al., 2010;  
215 Schofield et al., 2010). The measured data are used to verify the computational results in  
216 this study. In fact, they have been widely used in previous studies (Glenn et al., 2016; Seroka  
217 et al., 2016; Seroka et al., 2017).

218 HF Radars in the Mid-Atlantic Regional Association's Coastal Ocean Observing  
219 System are able to observe the surface currents. The recorded data have a temporal  
220 resolution of 1 hr and a spatial resolution of 6 km, and are assumed to be measured at an  
221 effective depth of around 2.7 m below the ocean surface based on Roarty et al. (2020). The  
222 data cover the MAB area from the coast to the shelf break. HF Radar measures the radial  
223 component of ocean surface currents based on the Doppler effect. The surface currents are  
224 determined by combining overlapping radials from different radars in the observational  
225 network using an optimal interpolation method (Roarty et al., 2010; Zhang et al., 2018).  
226 'Coverage' is defined to represent how many overlapping radials are combined, and is thus  
227 closely related to the accuracy of data at a given point. Previous studies pointed out that the  
228 data are rather reliable when the 'coverage' is larger than 90% (Roarty et al., 2010; Kohut  
229 et al. 2012). Intrinsic HF Radar uncertainty has been estimated to be in the order of 5 cm/s  
230 (Brunner and Lwiza, 2020), indicating a relatively error of around 0.10 in regards to the  
231 surface current velocities. When compared with ADCP, the RMS difference of HF Radar is  
232 only within 8 cm/s (Roarty et al., 2010; Kohut et al. 2012; Roarty et al. 2020). In this study,  
233 HF Radar data are directly obtained from <https://maracoos.org/> and spatially interpolated to  
234 the locations of our interest. All the data within the shelf break are found to be quite reliable  
235 since the 'coverage' there is larger than 90%. Note that the data outside the shelf break has  
236 a low coverage of 60%-90%. Though we use all the data as they are, we must remind that  
237 the data outside the shelf break should be viewed with caution.

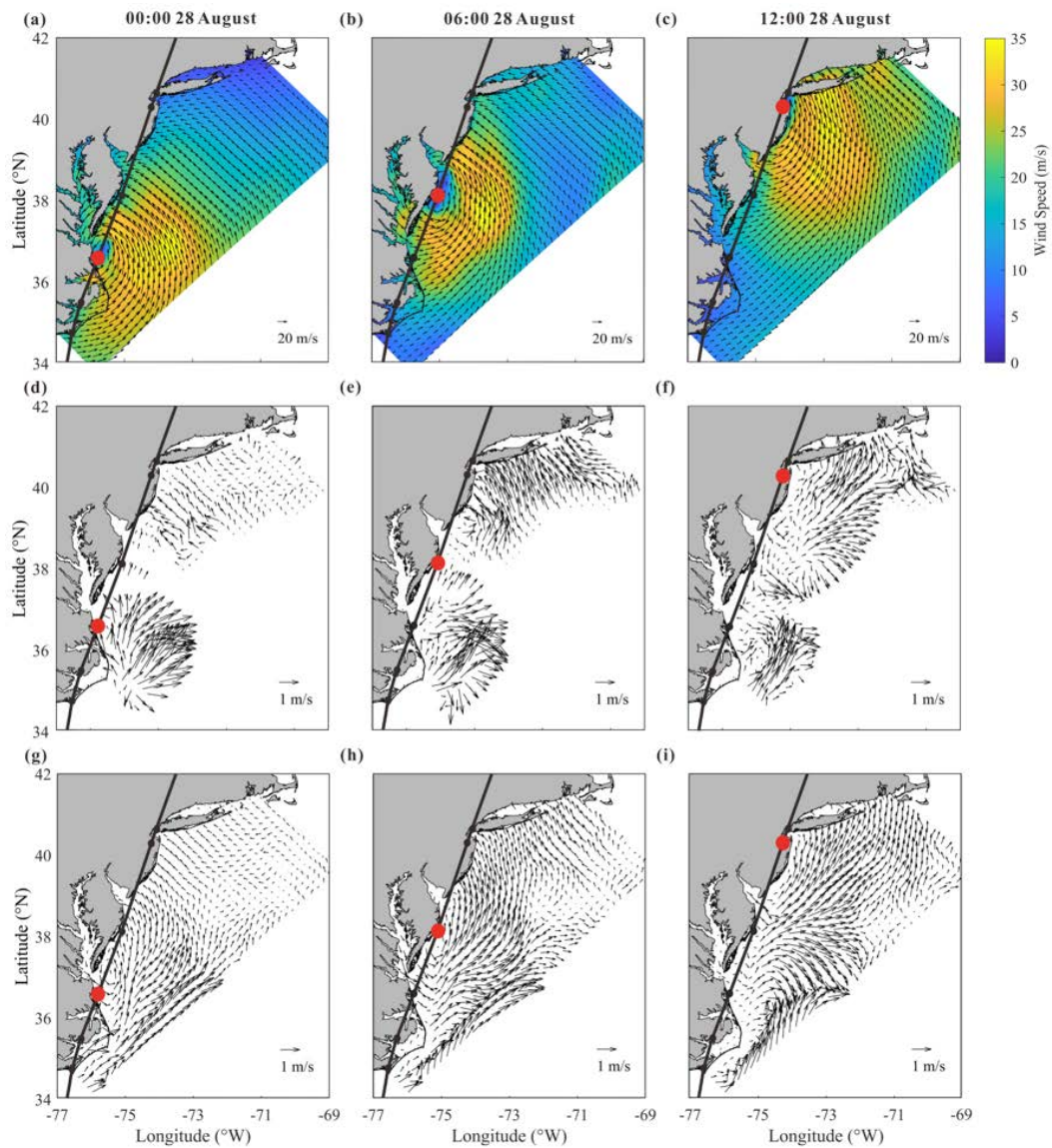
238 Glider RU16 was an autonomous underwater vehicle of the Rutgers Slocum glider  
239 (Schofield et al., 2007, 2010) platform developed by Teledyne-Webb Research, and has  
240 demonstrated to be advantageous in marine monitoring, particularly under extreme weather

241 conditions (Glenn et al., 2016; Miles et al., 2017; Zhang et al., 2018). It was equipped with  
242 the Seabird un-pumped conductivity, temperature, and depth (CTD) sensor, and could thus  
243 measure not only the vertical profiles of the seawater temperature and the salinity but also  
244 the water depth. It was programmed to move vertically through the water column, collect  
245 data every 2 s, and surface at a 3 h interval to provide high temporal resolution data  
246 (Schofield et al., 2007; Glenn et al., 2016; Seroka et al., 2016). The RU16 dataset has been  
247 widely used and well verified by previous authors (Glenn et al., 2016; Seroka et al., 2016;  
248 Seroka et al., 2017). Therefore, it is used as it is in this study. The dataset is available at  
249 <https://tds.marine.rutgers.edu/thredds/dodsC/cool/glider>.

## 250 **3 Ocean Responses to Hurricane Irene**

### 251 3.1 Effect of hurricane on ocean surface flow

252 As shown in Figure 1, Hurricane Irene (2011) entered the Mid-Atlantic Bight (MAB)  
253 area of the present interest at Cape Lookout, North Carolina as a Category-1 event at 12:00,  
254 27 August, 2011 (UTC time, the same below) with a maximum sustained wind (MSW) of  
255 over 38 m/s. It continued to move northeastward and made a landfall at Atlantic City, New  
256 Jersey at 9:35, 28 August with a MSW of around 30 m/s. During its motion in the MAB area  
257 of our interest, the radius of the hurricane wind field (the area with wind speed  $\geq 32.9$  m/s)  
258 reached a large value of 140 km (Avila and Cangialosi, 2011).  
259



260

261 Figure 2. Snapshots of (a-c) the 10-m wind provided by H\*WIND, (d-f) computed current  
 262 velocity of the surface layer and (g-i) observed current velocity of the surface layer, at (left  
 263 column) 00:00, (middle column) 06:00 and (right column) 12:00, 28 August, during the  
 264 passage of Hurricane Irene (2011). Note that best track of the hurricane reported by Avila  
 265 and Cangialosi (2011) is shown by black lines while the hurricane center is shown by red  
 266 circles.

267

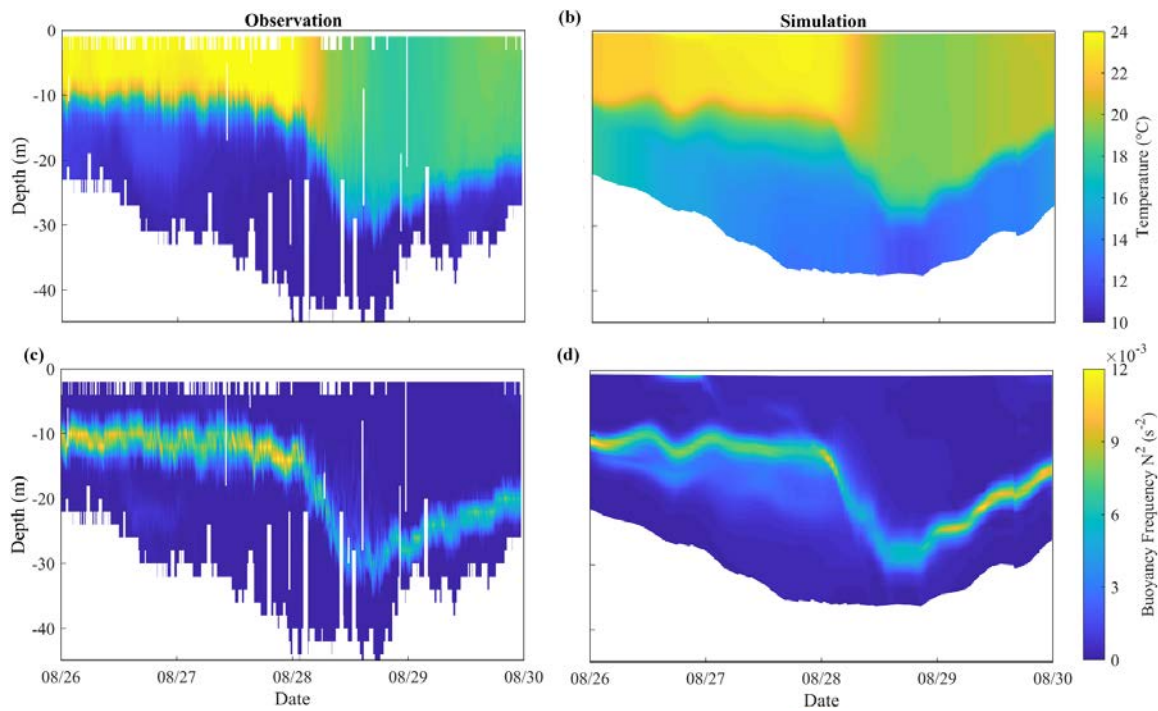
268 Figure 2 provides the snapshots of the wind, the computed and observed currents in  
 269 the MAB area at 00:00, 06:00 and 12:00, 28 August, 2011, respectively. Note that 00:00 and  
 270 12:00 correspond to the time when Hurricane Irene entered and left the area of our interest,  
 271 respectively. The wind field is plotted from the H\*WIND data, while the field currents are  
 obtained by the HF Radars and detided with Matlab toolbox T\_TIDE (Pawlowicz et al.,

272 2002).

273 The computed current velocity of the surface layer, as shown in Figure 2d-f, is  
274 compared with the observed one, as shown in Figure 2g-i, to verify the reliability of the  
275 numerical model presented in this study. At 00:00, 28 August, it is numerically demonstrated  
276 that currents rotating counterclockwise with a magnitude of over 1 m/s are rapidly generated  
277 by the wind near the hurricane center (Figure 2d). In the observed results, though there are  
278 significant data missing near the hurricane center, northeastward currents can still be  
279 identified on the offshore waters along North Carolina coast (Figure 2g) and are in  
280 reasonable agreement with the computed current field. Moreover, both computational and  
281 observational results support a fact that the onshore wind (Figure 2a) on the front side of the  
282 hurricane drives an onshore current with magnitude of 0.4 m/s along the northern MAB,  
283 especially in the nearshore area of New Jersey (Figure 2d and 2g). At 06:00, Hurricane Irene  
284 arrived at the offshore waters of Delmarva Peninsula. In spite of the field data missing, the  
285 rotating currents induced by the hurricane wind can be clearly recognized in both computed  
286 and observed results in the nearshore area of New Jersey (Figure 2e and 2h). In addition,  
287 relatively strong onshore currents with magnitude of over 1 m/s are observed near Long  
288 Island and are also well represented in the numerical results (Figure 2e). At 12:00, i.e., the  
289 time when the hurricane left the area of our interest, the counterclockwise rotating currents  
290 are still formed near the hurricane center as demonstrated by both computational and  
291 observational results (Figure 2f and 2i). At the same time, clockwise rotating currents are  
292 shown to be generated near Delmarva Peninsula in southern MAB after the hurricane passed  
293 over. This fact is certainly confirmed by both computed and observed results, indicating  
294 near inertial currents are activated after the hurricane event. Therefore, it becomes evident  
295 that the rotating wind of the hurricane immediately forces a rotating current in the surface  
296 layer of the ocean and induces an inertial current rotating in the opposite direction shortly  
297 after the hurricane passed over. It is also worthwhile to emphasize that, in general, the  
298 numerical results obtained with the present model agree fairly well with observed data.

299 3.2 Effect of hurricane on vertical stratification and sea surface cooling

300 Shown in Figure 3a is the vertical profile of the seawater temperature measured by  
301 Glider RU16 launched off the New Jersey Coast. It provides a good chance for us to validate  
302 the response of stratification to the hurricane event, which is likely one of the most important  
303 results of hurricane-ocean interaction. In Figure 3a, it is seen that the mixed layer off New  
304 Jersey coast was quite thin, with a thickness of less than 10 m, before the hurricane event.  
305 A strong stratification was clearly formed over a water depth of 40 m, with a surface  
306 temperature of 24 °C and a bottom temperature of 10 °C. When the hurricane center passed  
307 over the position of Glider RU16 at around 09:30, 28 August, the thickness of the mixed  
308 layer rapidly increased to nearly 30 m while the surface temperature was decreased by more  
309 than 5 °C, indicating a strong mixing process has occurred. By plotting the time series of  
310 the squared buoyancy frequency  $N$  based on the measured data, expansion of the mixed  
311 layer due to the hurricane event may be more vividly demonstrated (Figure 3c).  
312

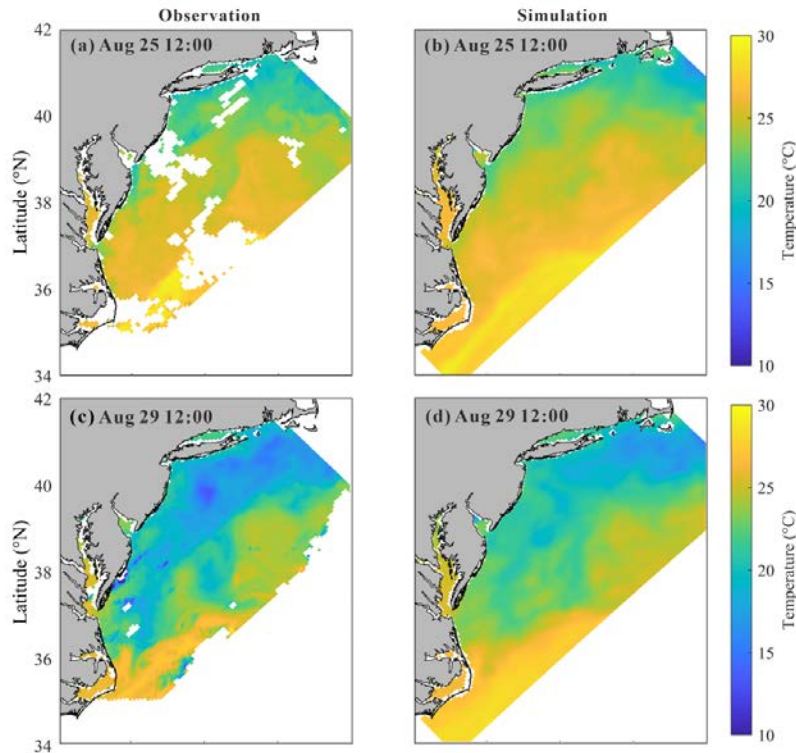


313  
314 Figure 3. Time series of the vertical profiles of (top row) the temperature and (bottom row)  
315 the squared buoyancy frequency, obtained from (a, c) Glider RU16 and (b, d) numerical  
316 model.  
317

318 Figure 3b and 3d present the computed results for the vertical distribution of seawater  
319 temperature obtained by virtually setting a measuring point moving with the glider in the  
320 real situation. The numerical results show a similar variation of the stratification pattern as  
321 observed before and during the hurricane event. They reproduce both extension of the mixed  
322 layer and cooling of the sea surface, indicating that the numerical model is capable of  
323 describing the development and destruction of ocean stratification. However, a sea surface  
324 cooling of about 4 °C obtained by the numerical model is a little smaller than 6-7 °C  
325 observed by the glider in the field, probably due to the inaccurate setting of the initial bottom  
326 temperature in the computation. Discrepancies of the squared buoyancy frequency  $N$  was  
327 also found in the thermocline (Figure 3c), where the temperature varied most dramatically.  
328 They are probably caused by the inaccurate setting of the initial temperature profile. In fact,  
329 the initial condition for the bottom temperature in HYCOM is somehow higher (about 4°C)  
330 than the observed value in the field if Figures 3a and 3b are compared. To correct this system  
331 error, the real-time profile obtained from RU16 is used for a nudging process in computation,  
332 i.e., the model temperature and salinity fields are forced to nudge toward observed data (see  
333 Thyng et al. (2021) for detailed description).

334 The sea surface temperatures (SST) before and after the hurricane event are further  
335 compared in Figure 4 (obtained from The Advanced Very High Resolution  
336 Radiometer (AVHRR), <https://earth.esa.int/eogateway/catalog/avhrr-level-1b-local-area-coverage-imagery>). Before the hurricane event, both observed and computed SST show  
337 similar patterns, i.e., the SST decreases with the increasing latitude. After the hurricane  
338 passage, the strong mixing and cooling mainly take place in shallow waters, where the initial  
339 stratification is strong (Zhang et al., 2016), especially near New Jersey and Long Island.  
340 However, the cooling is not prominent in shallow waters near North Carolina. In fact, it has  
341 been reported that the SST in this region had decreased and then recovered to its pre-  
342 hurricane level within only 1 day (Seroka et al., 2016). In fact, the HYCOM data showed  
343 that the initial bottom temperature near North Carolina was as high as 18 °C. Considering  
344 that sea surface cooling was positively related to the vertical temperature gradient (Shay and  
345

346 Brewster, 2010; Vincent et al., 2012; Zhang et al., 2016), the small amount of cold pool  
347 water in this region may have caused insignificant cooling and fast recovering.  
348



349  
350 Figure 4. Sea surface temperature at Aug 25 12:00, before the hurricane event (top row) and  
351 at Aug 29 12:00, after the hurricane event (bottom row) from (a, c) observed data and (b, d)  
352 numerical model.

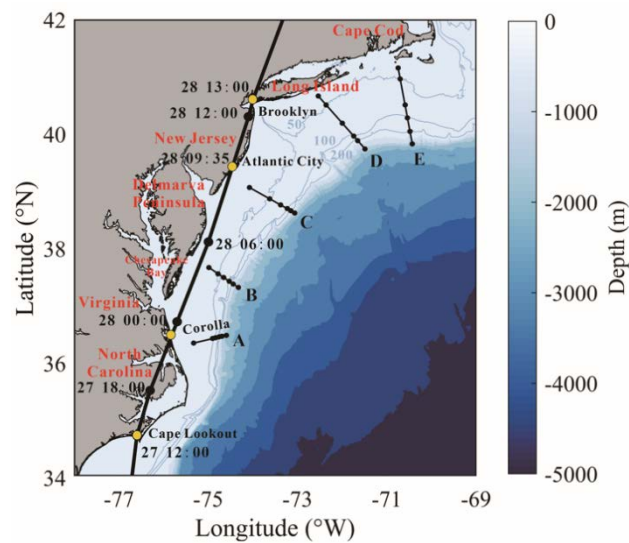
353

354 It should be pointed out that the computed SST cooling is 3-4 °C smaller than the  
355 observed one, which could also be explained by the inaccurate initial condition obtained  
356 from HYCOM. The HYCOM bottom temperature is somehow higher than actual, which  
357 could lead to the underestimation of the SST cooling. Therefore, we use the real-time SST  
358 data obtained from AVHRR for nudging process in computation to correct this system error  
359 (Thyng et al., 2021), considering that the accuracy of the initial stratification could  
360 obviously affect the modeling of mixing process. Note that the error is mainly caused by the  
361 discrepancy in initial settings but not the defects in numerical method. Thus this error could  
362 be calibrated in certain extent and thus would not affect the reliability of subsequent analysis,  
363 e.g. energy budget analysis.



364 3.3 Characteristics of NIC

365 To have a general understanding of the NICs in the MAB area induced by Hurricane  
366 Irene (2011), a network of 30 stations aligned on 5 cross-shore sections from south to north  
367 is introduced in this study to cover the area of our interest as shown in Figure 5, similar to  
368 Zhang et al (2018). In each section, 6 stations are placed in the cross-shore direction from  
369 the shore side to the deep ocean, where water depths are around 30 m, 50 m, 75 m, 120 m,  
370 and 220 m and 1000 m, respectively. Note that the most offshore stations are located outside  
371 the shelf break.



372  
373 Figure 5. Five virtual sections marked by short black lines.  
374

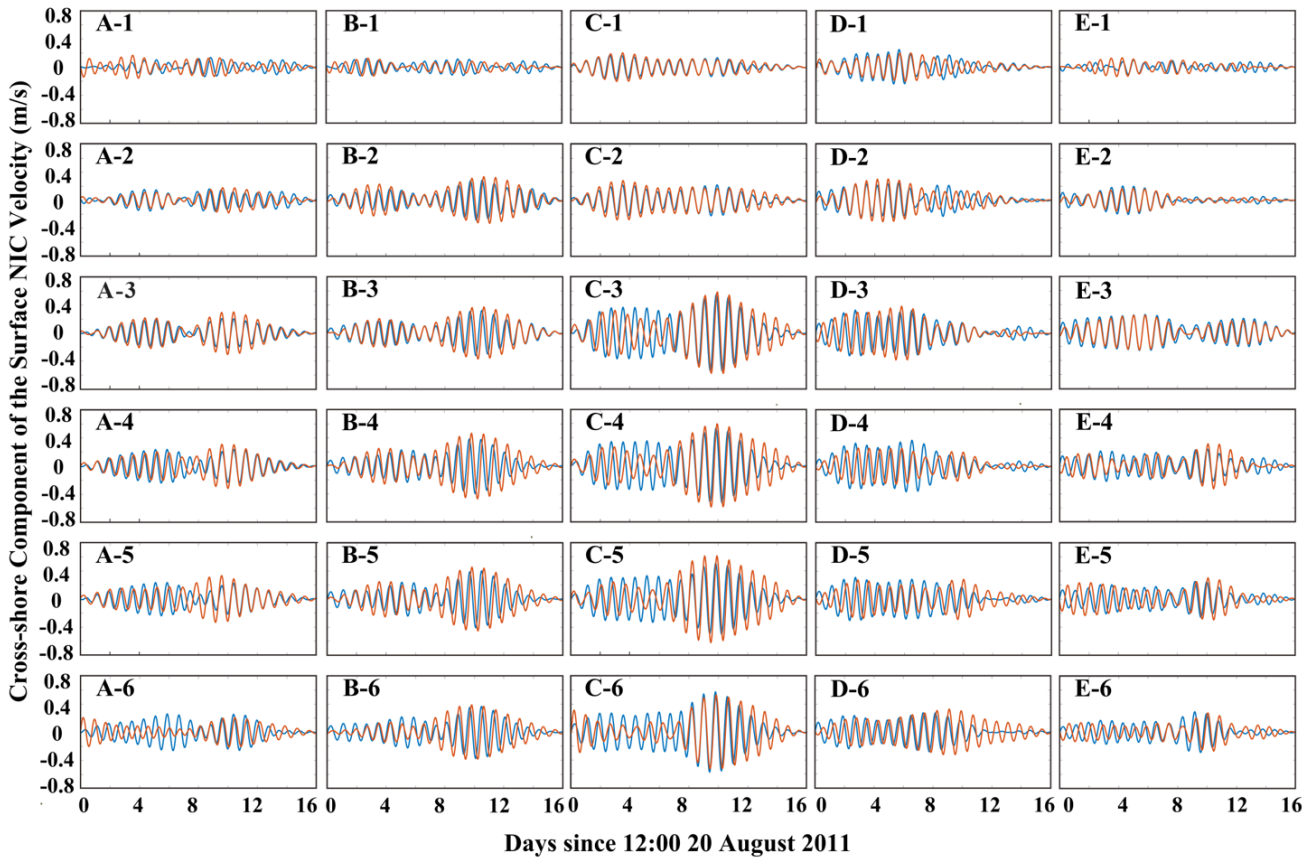
375 The velocity of NIC is obtained from the total current velocity by first excluding the  
376 tidal components and then passing it through a Butterworth filter with the frequency band  
377 of  $0.8-1.2 f_0$ , an effective approach proposed by Hormann et al. (2014), Zhang et al. (2018)  
378 and Kawaguchi et al. (2020). Shown in Figure 6 are the time series of surface velocity of  
379 the NIC component in the cross-shore direction interpolated to 30 stations during the time  
380 period of our study (16 days from 20 August to 5 September). Results obtained with the  
381 numerical model are also presented. The alongshore component is similar to cross-shore  
382 component and thus omitted here. Intuitively, the numerical results are in reasonably good  
383 agreement with the HF Radar data. For a further discussion we define the near inertial  
384 kinetic energy (NIKE) in the following way:

385 
$$E' = \frac{1}{2} \rho_0 |\mathbf{u}'|^2 \quad (13)$$

386 where,  $\rho_0$  is the velocity of the NIC;  $\mathbf{u}'$  is the seawater density at the standard  
 387 atmospheric pressure. A phased corrected relative mean square error may then be introduced  
 388 to describe the difference between the computed and observed NIKE:

389 
$$\Delta = \frac{\min_{\tau} \int_{t_0}^{t_1} [E'_o(t) - E'_c(t - \tau)]^2 dt}{\sqrt{\int_{t_0}^{t_1} [E'_o(t)]^2 dt} \sqrt{\int_{t_0}^{t_1} [E'_c(t)]^2 dt}} \quad (14)$$

390 where  $E'_o(t)$  and  $E'_c(t)$  are the observed and computed NIKE time series, respectively;  
 391  $[t_0, t_1]$  is the duration when the hurricane-induced NICs are prominent, which is taken to be  
 392 from August 25 to September 4 in this study;  $\tau$  is a time shift for eliminating the phase  
 393 error. We calculate  $\Delta$  at all 30 stations. It is shown that  $\Delta$  varies from 0.14-0.23 in most  
 394 stations where the coverage is larger than 90%. However, it is also necessary to mention  
 395 that in several nearshore stations, i.e. A1, D1 and E1,  $\Delta$  exceeds 0.3, because the NIC is  
 396 too weak at these stations as compared to the background currents. At the 6 stations outside  
 397 the shelf break, i.e., at A6, C6 and D6,  $\Delta$  even exceeds 0.5-0.6, implying that the HF Radar  
 398 data is less accurate outside the shelf with low ‘coverage’. As we mentioned in Section 2.3,  
 399 the relative RMS difference of HF Radar data is around 0.10. Taking this intrinsic HF Radar  
 400 uncertainty into consideration,  $\Delta = 0.14-0.23$  in our study is quite acceptable. Therefore,  
 401 we could conclude that our numerical results are in reasonably good agreement with the HF  
 402 Radar data. Inaccuracy in the numerical results of the NICs may come from the minor errors  
 403 in the wind forcing data because they are very sensitively related, e.g., underestimation at  
 404 C3-C6 before the hurricane event may come from the errors in low-resolution NAM data  
 405 used in pre-hurricane periods. In addition, error in the initial wind data may cause  
 406 insignificant phase discrepancies in B3-B6.

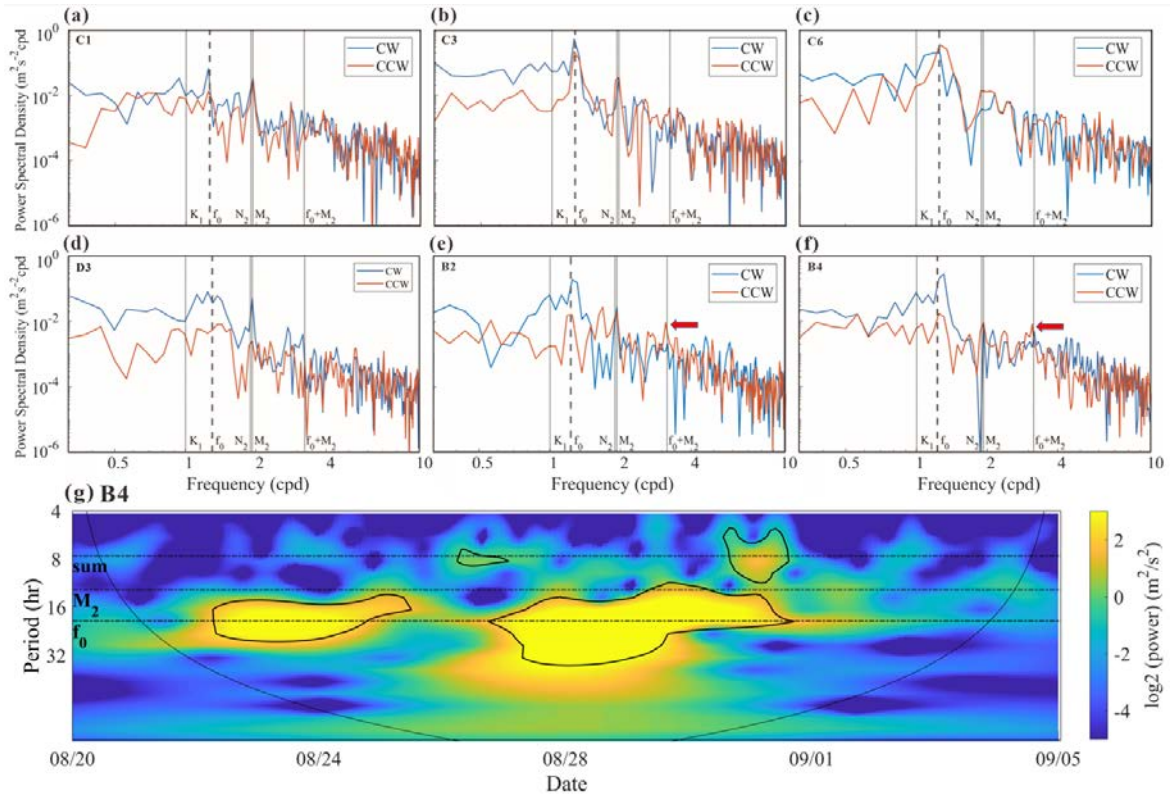


408 Figure 6. Time series of the NIC velocity in the surface layer obtained (blue line) by the HF  
 409 Radar and (orange line) with numerical model at 30 stations along sections A-E.  
 410

411 In Figure 6, it can be readily recognized that, in the cross-shore direction from shallow  
 412 to deep waters (i.e., Station No.1-No.5 in present study), the NIC velocity gradually  
 413 increases by a factor of at least three, e.g., from 0.15 m/s to 0.6 m/s in section C, which is  
 414 consistent with conclusions in previous studies (Kim and Kosro, 2013; Yang et al., 2015;  
 415 Rayson et al., 2015; Zhang et al., 2018). This is because that NIC velocity in the nearshore  
 416 region are restricted due to a combination of several reasons presented by Chen and Xie  
 417 (1997), Rayson et al. (2015) and Chen et al. (2017). Different from other studies, however,  
 418 the NIC velocity in the deep waters (i.e., Station No. 6 in the present study) is found to be  
 419 not larger or even smaller than that nearby the shelf break. This is probably due to that fact  
 420 that the track of Hurricane Irene (2011) was nearly attached to the shore during its motion  
 421 in the area of our interest and the wind stress over the deep ocean was relatively small. From  
 422 south to north, it is found that the NIC velocity in the middle regions, such as along section

423 C, is larger than those in south and north. By checking the numerical results, it is found that  
424 the stratification was only slightly destroyed during the hurricane event near section C as  
425 compared to the adjacent sections, which thus provided a better environment for NIC  
426 generation (Yang et al., 2015; Shen et al., 2017).

427 To evaluate the relative importance of the near inertial currents, the rotary spectra of  
428 the surface current velocity during the period of study (16 days) at different stations are  
429 shown in Figure 7. The tidal flows corresponding to the major constituents M2, N2 and K1,  
430 obtained with ADCIRC, are also plotted. It is seen that the velocity of the NICs is of an  
431 equivalent magnitude to that of the M2 tidal current at the shallow-water stations where the  
432 water depth is about 30 m (section C was taken for an example, Figure 7a). But, the velocity  
433 of the NICs is significantly larger than that of the tidal current in deeper regions (Figure 7b,  
434 c). It may be necessary to point out that weak NICs are not limited to the most nearshore  
435 stations. In section D, for example, it is extended to a water depth of 75 m (Station D3,  
436 Figure 7d) due to the severe destruction of stratification. However, the stratification outside  
437 D3 was relatively well maintained due to the thicker mixed layer in these regions and the  
438 farther distance from the main hurricane track. As discussed in the previous subsection, the  
439 weak NICs in the nearshore area are closely related to the destruction of stratification by the  
440 strong mixing process associated to the hurricane event (Yang et al., 2015; Shen et al., 2017).  
441 However, this effect does not challenge the dominant role of NICs in deep waters.



442

443

444

445

446

447

448

449

450

451

452

453

454

455

456

457

458

459

460

Figure 7. The rotary spectra of the current velocity in the surface layer during the simulation time (16 days) obtained by HF Radar at Stations (a) C1 (~30m), (b) C3 (~75m), (c) C6 (~1000 m), (d) D3, (e) B2 and (f) B4. Clockwise and counter-clockwise components of the current are shown by blue and orange lines, respectively (NICs are considered to be dominated by the clockwise component). The frequencies of the major tidal constituents M2, N2 and K1, the inertial frequency  $f_0$ , and the sum-frequency of M2 and  $f_0$  are all marked by gray lines. (g) Wavelet power spectrum for 10-30 m depth-averaged alongshore current component at Station B4 (see Thiebaut and Vennell (2010) for detailed description). Black contours indicate the 5% significance level against red noise and the arc line indicate the cone of influence.

Previous studies reported the nonlinear wave-wave interaction could transfer energy from the M2 tide and NIC into a wave at the sum of their frequencies ( $f_{M2}$ ). The key mechanism is the coupling between the vertical shear in NIC and the vertical velocity due to the internal tide (Davis and Xing, 2003; Hopkins et al., 2014; Shen et al., 2017; Wu et al., 2020). Though the M2 tide is rather strong in shallow waters during the hurricane event (Figure 7), nonlinear wave-wave interaction between the tidal current and the NIC could be hardly identified in most part of MAB. Nevertheless, a peak of the energy spectrum seems

461 to appear at the sum-frequency fM2 for the surface velocity at Stations B1 to B4, near  
462 Delmarva Peninsula (B2 and B4 were taken as examples in Figure 7e, f). The evolution of  
463 energy power at different frequencies for the middle-layer averaged (i.e., 10-30 m) currents,  
464 where the flow shear is concentrated, is further demonstrated based on wavelet analysis  
465 (Station B4 was taken as an example in Figure 7g). A peak energy at the sum-frequency fM2  
466 is clearly identified after the hurricane passage. In fact, the subsequent Section 4.2 in this  
467 paper will show that the strongest shear is found in offshore waters between Delmarva  
468 Peninsula and New Jersey, i.e., near sections B and C (Figure 9a). Besides, Brunner and  
469 Lwiza (2020) indicated that the most prominent M2 tide in southern MAB is located off  
470 Delmarva Peninsula (near section B), according to a long-term observed data. Therefore,  
471 the vertical shear in NIC and the vertical velocity due to the M2 tide is more likely to be  
472 coupled in this region (i.e., near section B). However, this interaction only occurs in limited  
473 regions and thus would not influence the NIC evolution in most part of MAB.

## 474 **4 Near Inertial Kinetic Energy**

### 475 **4.1 Conservation of NIKE**

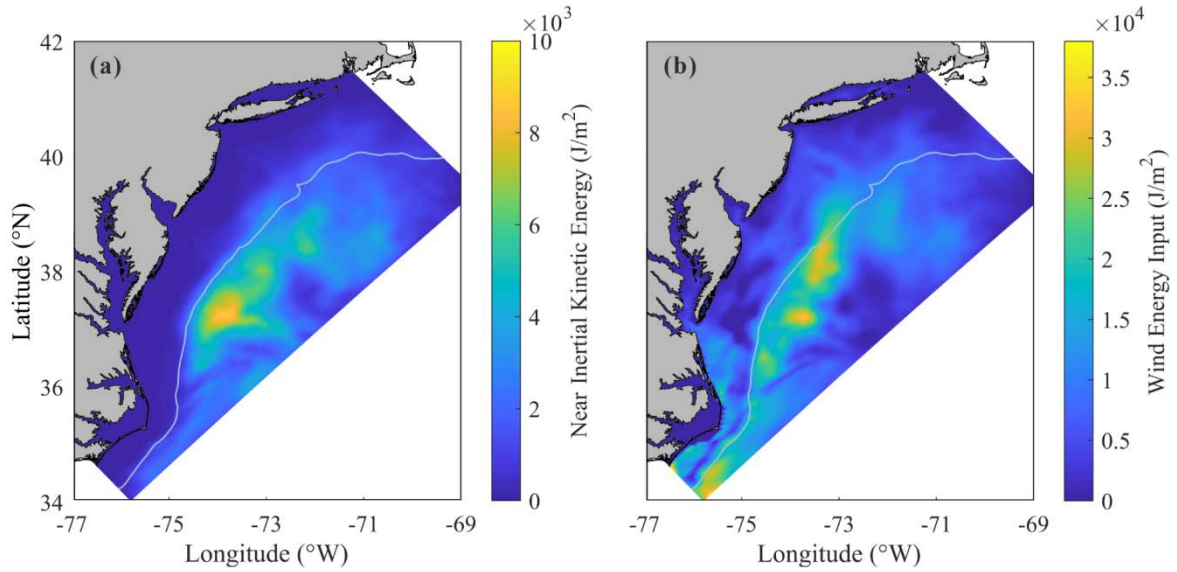
476 For description of the intensity of a NIC, the near inertial kinetic energy (NIKE) may  
477 be defined in Eq. (13). Note that the NIKE is mainly gained from the wind power and  
478 dissipated due to a few mechanisms. Evolution of the vertically integrated NIKE within a  
479 water column from the sea bottom to the ocean surface is thus governed by (Zhai et al., 2009)

$$480 \int_{-d}^{\eta} \frac{\partial E'}{\partial t} dz = \boldsymbol{\tau}_s \cdot \mathbf{u}'_s + \boldsymbol{\tau}_b \cdot \mathbf{u}'_b - \int_{-d}^{\eta} \rho_0 \nu_e \left| \frac{\partial \mathbf{u}'}{\partial z} \right|^2 dz - \int_{-d}^{\eta} \nabla \cdot (\mathbf{u}' p') dz - \int_{-d}^{\eta} \rho' g w' dz - \int_{-d}^{\eta} \nabla \cdot (\mathbf{U} E') dz + \text{others} \quad (15)$$

481 where,  $\mathbf{u}'_s$  and  $\mathbf{u}'_b$  are near inertial velocities at sea surface and bottom, respectively;  $\mathbf{U}$   
482 is the sub-inertial velocity;  $\rho'$  is the perturbation density, defined by  $\rho' = \rho - \rho_*$ ;  $\rho_*$  is  
483 the reference density, i.e., the density corresponding to a flattened stratification where the  
484 fluid is redistributed adiabatically to a stable and vertically uniform state from the actual  
485 condition (Holliday and McIntyre, 1981; Kang and Fringer, 2010; MacCready and Giddings,

486 2016);  $p'$  is the perturbation pressure, defined by  $p' = g \int_z^\eta \rho' dz$ . Terms on the right-hand  
487 side of Eq. (13) are the wind energy input, the dissipation due to bottom friction, the vertical  
488 diffusion due to turbulence, the horizontal divergence of near inertial energy flux, the  
489 conversion between kinetic and potential energy, and the advection of NIKE by the sub-  
490 inertial flow. The last term ‘others’ includes nonlinear transfer of energy between NICs and  
491 flows of other frequencies as well as the horizontal diffusion due to mixing. Note that the  
492 energy are integrated over the water column from  $z = -d$  to free surface  $z = \eta$ . In  
493 shallow waters,  $d$  is the actual water depth, while in deep waters,  $d$  is truncated to 200  
494 m (i.e., the depth of the shelf break). When the bottom boundary is set at  $z = -200$  m, the  
495 bottom friction vanishes in Eq. (13) but a term related to the downward energy flux, i.e.,  
496  $p'w' |_{z=-200m}$  should be added.

497 For a general understanding, distribution of the depth-integrated NIKE averaged over  
498 a 10-day period from August 25 to September 4 is presented in Figure 8a. The wind power  
499 integrated over the same period is plotted in Figure 8b. It is clearly shown in Figure 8a that  
500 the high NIKE region mainly located in the offshore waters of Delmarva Peninsula and New  
501 Jersey rather than in the nearshore area. This distribution pattern is rather similar to that of  
502 the wind energy input, as presented in Figure 8b, indicating that the NIKE was immediately  
503 gained from the wind power (Rayson et al. 2015; Shen et al., 2017; Zhang et al., 2018). In  
504 fact, the NIKE could also come from other processes apart from the wind energy input  
505 (Alford et al, 2016), meanwhile the wind energy input may also be transferred to energy of  
506 waves apart from NIC (Chen et al., 2017), which leads to differences between Figure 8a and  
507 7b.



508

509 Figure 8. Spatial distribution of (a) depth-integrated near inertial kinetic energy averaged  
 510 over the 10-day period and (b) wind power input to NICs integrated over the 10-day period.

511

512 Table 1. The contribution of each mechanism to energy budget. Percentages in parentheses  
 513 refer to the ratio of each factor to wind energy input.

Factor (J)	Contribution in Region A	Contribution in Region B
Wind Energy Input	$7.75 \times 10^{14}$	$3.16 \times 10^{14}$
Vertical Turbulence Diffusion	$3.12 \times 10^{14}$ (40%)	$2.12 \times 10^{14}$ (67%)
Lateral Divergence	$1.34 \times 10^{14}$ (17%)	$5.69 \times 10^{13}$ (18%)
Downward Transfer	$2.58 \times 10^{14}$ (33%)	0
Advection	$3.33 \times 10^{13}$ (4%)	$1.04 \times 10^{13}$ (3%)
Conversion	$6.9 \times 10^{12}$ (1%)	$1.58 \times 10^{13}$ (5%)
Bottom Friction	0	$7.58 \times 10^{13}$ (24%)

514

515 An important objective of the present study is to identify the mechanism of NIC  
 516 development and decay. For this purpose, we consider a rectangular domain and separate it  
 517 into deep water region A (depth > 200 m) and continental shelf region B (depth  $\leq$  200 m),  
 518 as depicted in Figure 1a. If the NICs are considered to be negligibly weak before and after

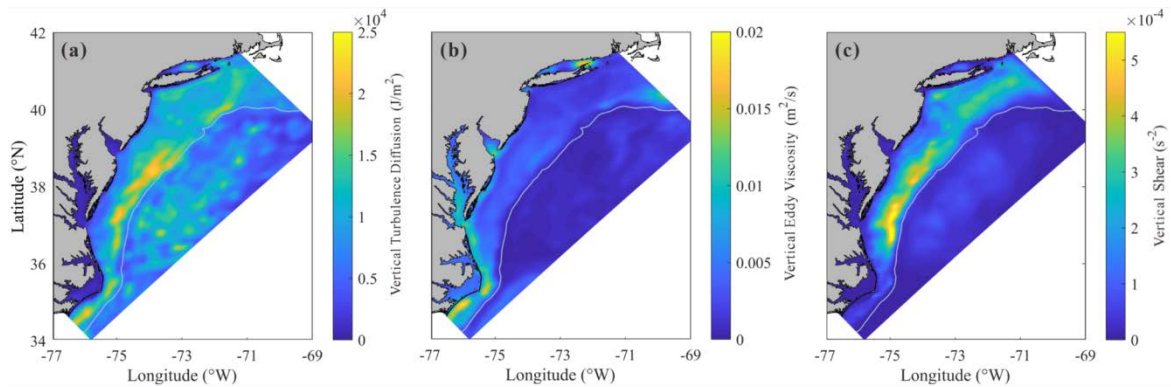


519 Hurricane Irene (2011), we may try to find how the wind power that drives the NICs during  
520 the hurricane event is balanced, by comparing the accumulated contribution of different  
521 mechanisms. Performing an integration of each terms in Eq. (13) with respect to time over  
522 10 days from August 25 to September 4 and with respect to the horizontal coordinates over  
523 both deep water region A and continental shelf region B, the contribution of each mechanism  
524 to the energy budget is obtained as shown in Table 1. It is clearly demonstrated that in the  
525 deep water region, the wind energy input was basically balanced by the vertical diffusion  
526 due to turbulence (40%) and a downward transfer of the near inertial energy to the deep  
527 ocean (33%). In the continental shelf region, the vertical diffusion due to turbulence  
528 dominated the dissipation of NIKE (nearly 70%), while the bottom friction played a  
529 secondary role (24%). It is worthwhile mentioning that lateral divergence of NIKE should  
530 not be neglected in both shallow and deep water regions under the hurricane condition  
531 (nearly 20%), different from previous studies which focused on NICs under the local wind  
532 condition or in a broader research region across the whole North Atlantic (Chant, 2001; Zhai  
533 et al., 2009; Shen et al., 2017). Other processes, e.g., advection due to sub-inertial flows,  
534 only played a minor role. Note that the ratio of near inertial energy decay to wind energy  
535 input exceeded 100% in the continental shelf region, confirming that NIKE may be gained  
536 from other sources in addition to wind energy input in nearshore regions (Alford et al., 2016).

#### 537 4.2 Decay of NIKE

538 The spatial distribution of the time-integrated energy dissipated through vertical  
539 diffusion due to turbulence is plotted in Figure 9a. It is seen that a large amount of the  
540 dissipation occurred at the offshore side of the continental shelf (i.e., at the offshore side of  
541 the shallow region B), which does not coincide with the region where the wind energy input  
542 is intense as demonstrated in Figure 8b. This implies that dissipation of NIKE is not mainly  
543 caused by an increased intensity of turbulence, which certainly takes place in a region where  
544 wind energy input achieves a high level (Zhai et al., 2009; Zhang et al., 2018). For a more  
545 detailed discussion, the averaged eddy viscosity  $\nu_e$  and the averaged vertical shear rate of  
546 NIC  $\left| \partial \mathbf{u}' / \partial z \right|^2$  during the period of our study are presented in Figure 9b and 8c. It is then

547 confirmed that the strong vertical shear also occurred at the outer half of the continental  
 548 shelf. The eddy viscosity, however, has a completely different distribution. In conclusion,  
 549 the vertical shear, known to be closely related to the ocean stratification (Shen et al., 2017),  
 550 plays a crucial role in the turbulence diffusion. It happened that one of the well-known  
 551 sharpest thermoclines in the world exists in the coastal water of MAB (Schofield et al., 2008;  
 552 Lentz, 2017). It may be necessary to emphasize that, although the stratification in the  
 553 shallowest water was totally destroyed during the hurricane event, as mentioned in Section  
 554 3, the seawater at the outer half of the continental shelf still partly maintained its  
 555 stratification.

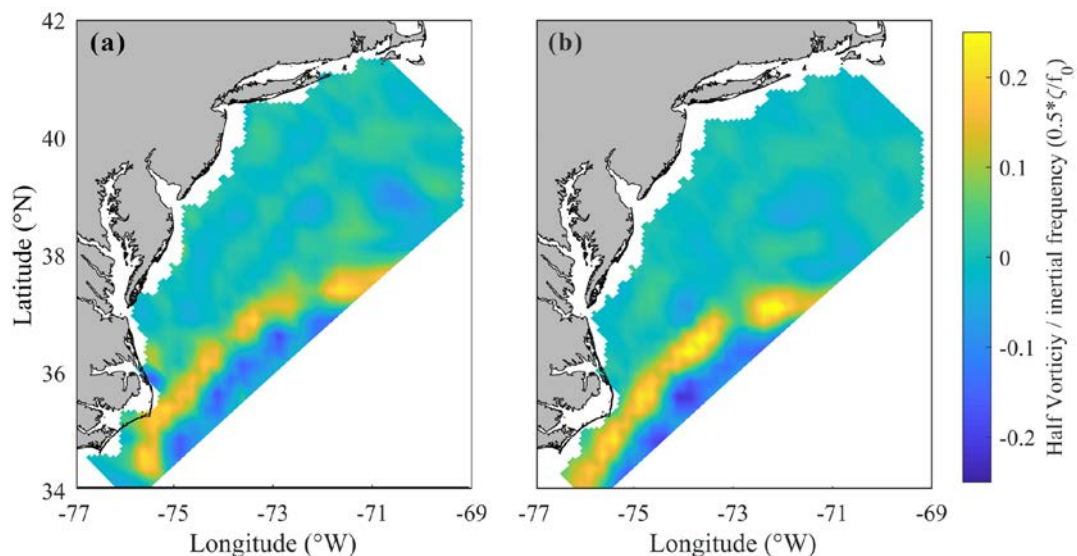


556  
 557 Figure 9. Spatial distribution of (a) depth-integrated vertical diffusion due to turbulence  
 558 integrated over the 10-day period, (b) depth-averaged vertical eddy viscosity and (c) depth-  
 559 averaged vertical shear, both averaged over the 10-day period.  
 560

561 The lateral divergence of NIKE flux, which also results in decay of NIKE and is not  
 562 trivial ( $\sim 20\%$ ) in both shallow and deep water regions, may have to be discussed in some  
 563 details. As shown in Eq. (13), the lateral divergence of NIKE flux is a vertical integration  
 564 of  $\nabla \cdot (\mathbf{u}'p')$ , which may also be expressed as an equivalent integration of  $\nabla \cdot (\mathbf{c}'E')$ ,  
 565 where  $\mathbf{c}'$  is the transport velocity of NIKE in the horizontal plane (Price, 1994). When  
 566 compared to previous studies (Zhai et al., 2009), which dealt with the normal wind induced  
 567 NIC over a large part of the North Atlantic and showed that the lateral divergence accounted  
 568 only for less than 5% of the total NIKE loss, we focused only on the hurricane-affected  
 569 region. In the hurricane-affected region, the larger NIKE gradient naturally leads to a larger  
 570 divergence. If we extend the domain of study by a factor of 1.5, however, contribution of

571 the averaged lateral divergence decreases by more than half. It is thus strongly implied that  
572 the lateral divergence of NIKE flux is significant within the hurricane-affected region.

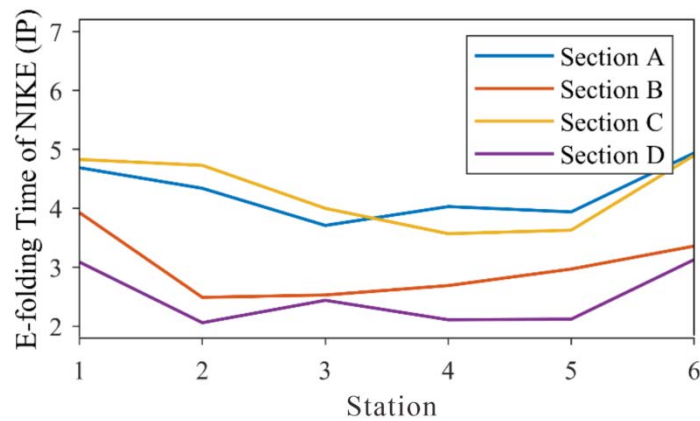
573 It is also of interest to note that the contribution of the lateral divergence in south region  
574 of our computational domain is less than 8%, much smaller than the average value of ~20%.  
575 Several studies have pointed out that the transport velocity  $c'$  is largely influenced by the  
576 background vorticity gradient (Zhai et al., 2009; Park et al., 2009). In other words, NIKE  
577 can hardly be transferred from a place of lower background vorticity to a place of higher  
578 background vorticity or, NIKE can hardly penetrate a vorticity ridge from either side. Shown  
579 in Figure 10 is the distribution of the background vorticity within our computational domain  
580 during the hurricane event (data from [https://resources.marine.copernicus.eu/product-](https://resources.marine.copernicus.eu/product-detail/SEALEVEL_GLO_PHY_CLIMATE_L4_MY_008_057/INFORMATION)  
581 [detail/SEALEVEL\\_GLO\\_PHY\\_CLIMATE\\_L4\\_MY\\_008\\_057/INFORMATION](https://resources.marine.copernicus.eu/product-detail/SEALEVEL_GLO_PHY_CLIMATE_L4_MY_008_057/INFORMATION)). A  
582 remarkable vorticity ridge exists in the southeast of the computational domain, which is  
583 considered to be caused by the strong horizontal shear at the edge of Gulf Stream (a warm  
584 and swift ocean current in Atlantic, flowing through the southern MAB and propagating  
585 northeastward). This vorticity ridge can reduce the lateral divergence of NIKE flux in south  
586 region of our computational domain.



587  
588 Figure 10. Spatial distribution of background vorticity (a) before the hurricane event on Aug  
589 25 and (b) after the hurricane event on Sep 4.  
590

591 4.3 Decay timescale of NIKE

592 It is of practical importance to determine the rate of NIKE decay. A conventional  
593 measure of the rate of NIKE may be its e-folding time, i.e., the timescale in which the NIKE  
594 decreases by a factor of e. Shown in Figure 11 is the e-folding time of the depth-integrated  
595 NIKE at 24 stations along sections A to D. The decay timescale in section E is not considered  
596 because this section is relatively far from the hurricane track as compared with other  
597 sections and also because the orientation of section E differs quite significantly from that of  
598 other sections.  
599



600  
601 Figure 11. The decay timescale of the depth-integrated NIKE at 24 stations along sections  
602 A to D. Note that the unit for the e-folding time is the inertial period.  
603

604 It is interesting to note that the decay timescales in the shallow and deep regions are  
605 fairly different. As shown in Figure 11, the NIKE is dissipated much more slowly outside  
606 the shelf break (Station No.6) than over the continental shelf. This difference is often  
607 considered to be an effect of the bottom friction and the extremely strong turbulence in the  
608 shallow waters, as pointed out by other researchers (Rayson et al., 2015; Shen et al., 2017).  
609 It is also interesting to find that the variation of NIKE decay rate in shallow waters is much  
610 more complicated than in the deep waters. In the cross-shore direction, the NIKE at the  
611 middle stations, i.e., Stations No. 3 to No. 5, located at the outer half of the continental shelf,  
612 is shown to be dissipated most rapidly, especially along sections A to C (Figure 11). This  
613 phenomenon is actually supported by the fact that the strongest turbulence diffusion

614 occurred over the outer half of the continental shelf, particularly in the relevant region  
615 between sections A and C (Figure 9a). Considering the variation of the wind energy input  
616 within the same section should not be too large, the ratio of turbulence diffusion to wind  
617 energy input must be mainly determined by the turbulence diffusion. Therefore, the strong  
618 turbulence dissipation due to the strong vertical shear in well-maintained stratification is  
619 responsible for the rapid energy decay in the outer half of the continental shelf, as shown in  
620 Section 4.2. Although the bottom friction also has some effect on the decay timescale of  
621 NIKE onshore, the turbulence effect is predominant.

622 In the alongshore direction, it is shown that the NIKE in sections B and D decayed  
623 more rapidly. Actually, the decay timescale there is only 2 to 3 inertial periods compared to  
624 4 to 5 inertial periods in sections A and C. However, the limited variability of the turbulence  
625 diffusion in alongshore direction should not lead to such a big difference. Near section A,  
626 the vorticity ridge in Gulf Stream restricted the lateral divergence of NIKE, which may  
627 contribute to a long decay timescale to some extent. However, the role of this effect was  
628 limited. In fact, as mentioned in Section 3, the nonlinear wave-wave interaction near section  
629 B may have caused a transfer of NIKE to other frequencies, as also pointed out by Shen et  
630 al. (2017). In fact, it is found that the ratio of turbulence diffusion to wind input in section  
631 B was larger than in other sections by 20%-30%, due to the low level of wind input (Figure  
632 8b) and high level of turbulence dissipation (Figure 9a) there. These factors combined seem  
633 to have yielded an extraordinarily short e-folding time in section B. In section D, due to the  
634 complete destruction of stratification after the hurricane event (as mentioned in Section 3  
635 and shown in Figure 7d), the NICs were of the same order as the background flow (D1-D4  
636 in Figure 6). Therefore, the decay timescale of NIKE in section D is certainly inaccurate  
637 and possibly meaningless.

## 638 **5 Conclusion**

639 This study is aimed to investigate the development and decay mechanism of NICs in  
640 the MAB area caused by Hurricane Irene (2011). Numerical results obtained with ROMS

641 are shown to agree well with the observational data. Both computational and observational  
642 results show that the rotating wind of the hurricane immediately forced a rotating current in  
643 the surface layer of the ocean and induced an inertial current rotating in the opposite  
644 direction about one inertial period after the hurricane passed over. The NICs overwhelmed  
645 M2 tide in most areas of the MAB region except in the nearshore area where the  
646 stratification was totally destroyed by the strong mixing due to turbulence. In addition, the  
647 cross-shore component of the NIC velocity gradually increases by a factor of at least three  
648 from a shallow-water position to the shelf break.

649 The energy budget in the NICs is investigated in both deep and shallow waters. NIKE  
650 was shown to be immediately gained from the wind power during the hurricane event. In  
651 the deep water region, NIKE was mainly dissipated by the vertical diffusion due to  
652 turbulence and partially transferred to deep waters. In the continental shelf region, NIKE  
653 was basically dissipated by the turbulence diffusion, meanwhile the bottom friction played  
654 a secondary role. The nonlinear wave-wave interaction only dissipated NIKE in limited  
655 regions, e.g. shelf waters off Delmarva Peninsula. Notably, the lateral divergence of NIKE  
656 should be taken into consideration in both shallow and deep water regions under the  
657 hurricane condition. However, in southern MAB, it was restricted by a vorticity ridge at the  
658 edge of Gulf Stream. It is also clarified that the NIKE dissipation due to turbulence diffusion  
659 is much more closely related to the rate of the vertical shear rather than the intensity of  
660 turbulence, which certainly takes place in a region where wind energy input achieves a high  
661 level. The strong vertical shear at the offshore side of the continental shelf led to the  
662 strong turbulence dissipation in this region.

## 663 **Acknowledgements**

664 This research is supported by National Natural Science Foundation of China (NSFC)  
665 under grant No. 11732008.

## 666 **Data Availability Statements**

667 The data used in this study are listed below. In particular, the regional oceanic modeling  
668 system (ROMS) code is available at <https://www.myroms.org>; HF radar data is available at  
669 [http://tds.marine.rutgers.edu/thredds/dodsC/cool/codar/totals/5Mhz\\_6km\\_realtime\\_fmrc/  
670 Maracoos\\_5MHz\\_6km\\_Totals-FMRC\\_best.ncd.html](http://tds.marine.rutgers.edu/thredds/dodsC/cool/codar/totals/5Mhz_6km_realtime_fmrc/Maracoos_5MHz_6km_Totals-FMRC_best.ncd.html); Glider data is available at  
671 [http://tds.marine.rutgers.edu/thredds/dodsC/cool/glider/mab/Gridded/20110810T1330\\_epa  
672 \\_ru16\\_active.nc.html](http://tds.marine.rutgers.edu/thredds/dodsC/cool/glider/mab/Gridded/20110810T1330_epa_ru16_active.nc.html); HYCOM data is available at [https://www.hycom.org/data/glbu0pt08/  
673 expt-91pt2](https://www.hycom.org/data/glbu0pt08/expt-91pt2); ADCIRC data is available at <https://adcirc.org/products/adcirc-tidal-databases>;  
674 USGS data is available at <https://waterdata.usgs.gov>; H\*WIND data is available at  
675 [https://www.aoml.noaa.gov/hrd/data\\_sub/wind.html](https://www.aoml.noaa.gov/hrd/data_sub/wind.html); NAM data is available at  
676 [https://www.ncdc.noaa.gov/data-access/model-data/model-datasets/north-american-  
677 mesoscale-forecast-system-nam](https://www.ncdc.noaa.gov/data-access/model-data/model-datasets/north-american-mesoscale-forecast-system-nam); C3S data is available at  
678 [https://resources.marine.copernicus.eu/product-detail/SEALEVEL\\_GLO\\_PHY  
679 \\_CLIMATE\\_L4\\_MY\\_008\\_057/INFORMATION](https://resources.marine.copernicus.eu/product-detail/SEALEVEL_GLO_PHY_CLIMATE_L4_MY_008_057/INFORMATION); AVHRR data is available at  
680 <https://earth.esa.int/eogateway/catalog/avhrr-level-1b-local-area-coverage-imagery>.

## 681 **References**

682 Alford, M.H., 2003a. Improved global maps and 54-year history of wind-work on ocean  
683 inertial motions. *Geophysical Research Letters*, 30(8).

684 Alford, M.H., 2003b. Redistribution of energy available for ocean mixing by long-range  
685 propagation of internal waves. *Nature*, 423(6936): 159-162.

686 Alford, M.H., MacKinnon, J.A., Simmons, H.L. and Nash, J.D., 2016. Near-inertial internal  
687 gravity waves in the ocean. *Annual Review of Marine Science*, 8(1): 95-123.

688 Allahdadi, M., 2014. Numerical experiments of hurricane impact on vertical mixing and de-  
689 stratification of the louisiana shelf waters. Ph. D. Thesis, Louisiana State University,  
690 Baton Rouge.

691 Amante, C. and Eakins, B.W., 2009. Etopo1 1 arc-minute global relief model: Procedures,  
692 data sources and analysis. NOAA Technical Memorandum NESDIS NGDC-24,

693 National Geophysical Data Center, NOAA.

694 Avila, L.A. and Cangialosa, J., 2011. Tropical cyclone report: Hurricane irene: August 21–  
695 28, 2011. National Hurricane Center Report AL0920011, US National Oceaninc and  
696 Atmospheric Administration's National Weather Service.

697 Brunner, K. and Lwiza, K.M.M., 2020. Tidal velocities on the mid-atlantic bight continental  
698 shelf using high-frequency radar. *Journal of Oceanography*, 76(4): 289-306.

699 Castelao, R.M., 2014. Mesoscale eddies in the south atlantic bight and the gulf stream  
700 recirculation region: Vertical structure. *Journal of Geophysical Research: Oceans*,  
701 119(3): 2048-2065.

702 Chang, S.W. and Anthes, R.A., 1978. Numerical simulations of the ocean's nonlinear,  
703 baroclinic response to translating hurricanes. *Journal of Physical Oceanography*,  
704 8(3): 468-480.

705 Chant, R.J., 2001. Evolution of near-inertial waves during an upwelling event on the new  
706 jersey inner shelf. *Journal of Physical Oceanography*, 31(3): 746-764.

707 Chassignet, E.P. et al., 2007. The hycom (hybrid coordinate ocean model) data assimilative  
708 system. *Journal of Marine Systems*, 65(1): 60-83.

709 Chen, C., Reid, R.O. and Nowlin Jr, W.D., 1996. Near-inertial oscillations over the texas-  
710 louisiana shelf. *Journal of Geophysical Research: Oceans*, 101(C2): 3509-3524.

711 Chen, C. and Xie, L., 1997. A numerical study of wind-induced, near-inertial oscillations  
712 over the texas-louisiana shelf. *Journal of Geophysical Research: Oceans*, 102(C7):  
713 15583-15593.

714 Chen, G., Xue, H., Wang, D. and Xie, Q., 2013. Observed near-inertial kinetic energy in the  
715 northwestern south china sea. *Journal of Geophysical Research: Oceans*, 118(10):  
716 4965-4977.

717 Chen, S., Chen, D. and Xing, J., 2017. A study on some basic features of inertial oscillations  
718 and near-inertial internal waves. *Ocean Science*, 13(5): 829-836.

719 Chen, Y. and Yu, X., 2016. Enhancement of wind stress evaluation method under storm  
720 conditions. *Climate Dynamics*, 47(12): 3833-3843.



721 Chen, Y., Zhang, F., Green, B.W. and Yu, X., 2018. Impacts of ocean cooling and reduced  
722 wind drag on hurricane katrina (2005) based on numerical simulations. *Monthly*  
723 *Weather Review*, 146(1).

724 Churchill, J.H., Wirick, C.D., Flagg, C.N. and Pietrafesa, L.J., 1994. Sediment resuspension  
725 over the continental shelf east of the delmarva peninsula. *Deep Sea Research Part II:*  
726 *Topical Studies in Oceanography*, 41(2): 341-363.

727 Cummings, J.A., 2005. Operational multivariate ocean data assimilation. *Quarterly Journal*  
728 *of the Royal Meteorological Society*, 131(613): 3583-3604.

729 D'Asaro, E.A., 1985. The energy flux from the wind to near-inertial motions in the surface  
730 mixed layer. *Journal of Physical Oceanography*, 15: 1043-1059.

731 Davies, A.M. and Xing, J., 2003. On the interaction between internal tides and wind-induced  
732 near-inertial currents at the shelf edge. *Journal of Geophysical Research: Oceans*,  
733 108(C3).

734 Derrick, T.R., Bates, B.T. and Dufek, J.S., 1994. Evaluation of time-series data sets using  
735 the pearson product-moment correlation coefficient. *Medicine and science in sports*  
736 *and exercise*, 26(7): 919-928.

737 Donelan, M.A. et al., 2004. On the limiting aerodynamic roughness of the ocean in very  
738 strong winds. *Geophysical Research Letters*, 31(18).

739 Dorostkar, A., Boegman, L., Diamessis, P. and Pollard, A., 2010. Sensitivity of mitgcm to  
740 different model parameters in application to cayuga lake. *Proceedings of the 6th*  
741 *International Symposium on Environmental Hydraulics, Two Volume Set*, p.^pp.  
742 373-378.

743 Emanuel, K.A., 1995. Sensitivity of tropical cyclones to surface exchange coefficients and  
744 a revised steady-state model incorporating eye dynamics. *Journal of the*  
745 *Atmospheric Sciences*, 52: 3969-3976.

746 Fairall, C.W., Bradley, E.F., Rogers, D.P., Edson, J.B. and Young, G.S., 1996. Bulk  
747 parameterization of air-sea fluxes for tropical ocean-global atmosphere coupled-  
748 ocean atmosphere response experiment. *Journal of Geophysical Research: Oceans*,

749 101(C2): 3747-3764.

750 Freeman, N.G., Hale, A.M. and Danard, M.B., 1972. A modified sigma equations' approach  
751 to the numerical modeling of great lakes hydrodynamics. *Journal of Geophysical*  
752 *Research* 77(6): 1050-1060.

753 Furuichi, N., Hibiya, T. and Niwa, Y., 2008. Model-predicted distribution of wind-induced  
754 internal wave energy in the world's oceans. *Journal of Geophysical Research:*  
755 *Oceans*, 113(C9).

756 Garrett, C., 2001. What is the “near-inertial” band and why is it different from the rest of  
757 the internal wave spectrum? *Journal of Physical Oceanography*, 31(4): 962-971.

758 Glenn, S.M. et al., 2016. Stratified coastal ocean interactions with tropical cyclones. *Nature*  
759 *Communications*, 7(1): 10887.

760 Gregg, M.C., 1987. Diapycnal mixing in the thermocline: A review. *Journal of Geophysical*  
761 *Research: Oceans*, 92(C5): 5249-5286.

762 Haidvogel, D.B. et al., 2008. Ocean forecasting in terrain-following coordinates:  
763 Formulation and skill assessment of the regional ocean modeling system. *Journal of*  
764 *Computational Physics*, 227(7): 3595-3624.

765 Hoarfrost, A. et al., 2019. Gulf stream ring water intrusion on the mid-atlantic bight  
766 continental shelf break affects microbially driven carbon cycling. 6.

767 Holliday, D. and McIntyre, M.E., 1981. On potential energy density in an incompressible,  
768 stratified fluid. *Journal of Fluid Mechanics*, 107: 221-225.

769 Hopkins, J.E., Stephenson Jr, G.R., Green, J.A.M., Inall, M.E. and Palmer, M.R., 2014.  
770 Storms modify baroclinic energy fluxes in a seasonally stratified shelf sea: Inertial-  
771 tidal interaction. *Journal of Geophysical Research: Oceans*, 119(10): 6863-6883.

772 Hormann, V., Centurioni, L.R., Rainville, L., Lee, C.M. and Braasch, L.J., 2014. Response  
773 of upper ocean currents to typhoon fanapi. *Geophysical Research Letters*, 41(11):  
774 3995-4003.

775 Jackett, D.R. and McDougall, T.J., 1995. Minimal adjustment of hydrographic profiles to  
776 achieve static stability. *Journal of Atmospheric and Oceanic Technology*, 12(2): 381-

777 389.

778 Janjic, Z.I. et al., 2004, June. The ncep wrf core, 20th Conference on Weather Analysis and  
779 Forecasting/16th Conference on Numerical Weather Prediction, Seattle, Washington,  
780 pp. 10-25.

781 Jochum, M. et al., 2013. The impact of oceanic near-inertial waves on climate. *Journal of*  
782 *Climate*, 26(9): 2833-2844.

783 Kang, D. and Fringer, O., 2010. On the calculation of available potential energy in internal  
784 wave fields. *Journal of Physical Oceanography*, 40(11): 2539-2545.

785 Kawaguchi, Y., Wagawa, T. and Igeta, Y., 2020. Near-inertial internal waves and multiple-  
786 inertial oscillations trapped by negative vorticity anomaly in the central sea of japan.  
787 *Progress in Oceanography*, 181: 102240.

788 Kim, S.Y. and Kosro, P.M., 2013. Observations of near-inertial surface currents off oregon:  
789 Decorrelation time and length scales. *Journal of Geophysical Research: Oceans*,  
790 118(7): 3723-3736.

791 Kohut, J., Roarty, H., Randall-Goodwin, E., Glenn, S. and Lichtenwalner, C.S., 2012.  
792 Evaluation of two algorithms for a network of coastal HF Radars in the Mid-Atlantic  
793 Bight. *Ocean Dynamics*, 62(6): 953-968.

794 Kunze, E., 1985. Near-inertial wave propagation in geostrophic shear. *Journal of Physical*  
795 *Oceanography*, 15(5): 544-565.

796 Lentz, S.J., 2017. Seasonal warming of the middle atlantic bight cold pool. *Journal of*  
797 *Geophysical Research: Oceans*, 122(2): 941-954.

798 Li, M., Zhong, L., Boicourt, W.C., Zhang, S. and Zhang, D.-L., 2007. Hurricane-induced  
799 destratification and restratification in a partially-mixed estuary. *Journal of Marine*  
800 *Research*, 65(2): 169-192.

801 MacCready, P. and Giddings, S.N., 2016. The mechanical energy budget of a regional ocean  
802 model. *Journal of Physical Oceanography*, 46(9): 2719-2733.

803 MacKinnon, J.A. and Gregg, M.C., 2005. Near-inertial waves on the new england shelf:  
804 The role of evolving stratification, turbulent dissipation, and bottom drag. *Journal*

805 of Physical Oceanography, 35(12): 2408-2424.

806 Marchesiello, P., McWilliams, J.C. and Shchepetkin, A., 2001. Open boundary conditions  
807 for long-term integration of regional oceanic models. *Ocean Modelling*, 3(1): 1-20.

808 Miles, T., Seroka, G. and Glenn, S., 2017. Coastal ocean circulation during hurricane sandy.  
809 *Journal of Geophysical Research: Oceans*, 122(9): 7095-7114.

810 Mulligan, R.P. and Hanson, J.L., 2016. Alongshore momentum transfer to the nearshore  
811 zone from energetic ocean waves generated by passing hurricanes. *Journal of*  
812 *Geophysical Research: Oceans*, 121(6): 4178-4193.

813 Munk, W. and Wunsch, C., 1998. Abyssal recipes ii: Energetics of tidal and wind mixing.  
814 *Deep Sea Research Part I: Oceanographic Research Papers*, 45(12): 1977-2010.

815 Olabarrieta, M., Warner, J.C. and Kumar, N., 2011. Wave-current interaction in willapa bay.  
816 *Journal of Geophysical Research: Oceans*, 116(C12).

817 Park, J.J., Kim, K. and Schmitt, R.W., 2009. Global distribution of the decay timescale of  
818 mixed layer inertial motions observed by satellite-tracked drifters. *Journal of*  
819 *Geophysical Research: Oceans*, 114(C11).

820 Pawlowicz, R., Beardsley, B. and Lentz, S., 2002. Classical tidal harmonic analysis  
821 including error estimates in MATLAB using T\_TIDE. *Computers & Geosciences*,  
822 28(8): 929-937.

823 Pollard, R.T., 1980. Properties of near-surface inertial oscillations. *Journal of Physical*  
824 *Oceanography*, 10(3): 385-398.

825 Powell, M.D., Houston, S.H., Amat, L.R. and Morisseau-Leroy, N., 1998. The hrd real-time  
826 hurricane wind analysis system. *Journal of Wind Engineering and Industrial*  
827 *Aerodynamics*, 77-78: 53-64.

828 Powell, M.D., Vickery, P.J. and Reinhold, T.A., 2003. Reduced drag coefficient for high  
829 wind speeds in tropical cyclones. *Nature*, 422(6929): 279-283.

830 Price, J.F., 1983. Internal wave wake of a moving storm. Part i. Scales, energy budget and  
831 observations. *Journal of Physical Oceanography*, 13(6): 949-965.

832 Price, J.F., Sanford, T.B. and Forristall, G.Z., 1994. Forced stage response to a moving

833 hurricane. *Journal of Physical Oceanography*, 24(2): 233-260.

834 Rayson, M.D. et al., 2015. Near-inertial ocean response to tropical cyclone forcing on the  
835 Australian north-west shelf. *Journal of Geophysical Research: Oceans*, 120(12):  
836 7722-7751.

837 Rimac, A., von Storch, J.-S., Eden, C. and Haak, H., 2013. The influence of high-resolution  
838 wind stress field on the power input to near-inertial motions in the ocean.  
839 *Geophysical Research Letters*, 40(18): 4882-4886.

840 Roarty, H. et al., 2010. Operation and application of a regional high-frequency radar  
841 network in the mid-atlantic bight. *Marine Technology Society Journal*, 44(6): 133-  
842 145.

843 Roarty, H. et al., 2020. Annual and seasonal surface circulation over the mid-atlantic bight  
844 continental shelf derived from a decade of high frequency radar observations.  
845 *Journal of Geophysical Research: Oceans*, 125(11): e2020JC016368.

846 Rodi, W., 1987. Examples of calculation methods for flow and mixing in stratified fluids.  
847 *Journal of Geophysical Research: Oceans*, 92(C5): 5305-5328.

848 Sanford, T.B., Price, J.F. and Girton, J.B., 2011. Upper-ocean response to hurricane frances  
849 (2004) observed by profiling em-apex floats. *Journal of Physical Oceanography*,  
850 41(6): 1041-1056.

851 Schofield, O. et al., 2008. The decadal view of the mid-atlantic bight from the coolroom: Is  
852 our coastal system changing? *Oceanography*, 21(4): 108-117.

853 Schofield, O. et al., 2007. Slocum gliders: Robust and ready. *Journal of Field Robotics*,  
854 24(6): 473-485.

855 Schofield, O. et al., 2010. A regional slocum glider network in the Mid-Atlantic Bight  
856 leverages broad community engagement. *Marine Technology Society Journal*, 44(6):  
857 185-195.

858 Seroka, G. et al., 2016. Hurricane Irene sensitivity to stratified coastal ocean cooling.  
859 *Monthly Weather Review*, 144(9): 3507-3530.

860 Seroka, G. et al., 2017. Rapid shelf-wide cooling response of a stratified coastal ocean to

861 hurricanes. *Journal of Geophysical Research: Oceans*, 122(6): 4845-4867.

862 Shay, L.K. and Brewster, J.K., 2010. Oceanic heat content variability in the eastern pacific  
863 ocean for hurricane intensity forecasting. *Monthly Weather Review*, 138(6): 2110-  
864 2131.

865 Shchepetkin, A.F. and McWilliams, J.C., 2005. The regional oceanic modeling system  
866 (roms): A split-explicit, free-surface, topography-following-coordinate oceanic  
867 model. *Ocean Modelling*, 9(4): 347-404.

868 Shearman, R.K., 2005. Observations of near-inertial current variability on the new england  
869 shelf. *Journal of Geophysical Research: Oceans*, 110(C2).

870 Shen, J., Qiu, Y., Zhang, S. and Kuang, F., 2017. Observation of tropical cyclone-induced  
871 shallow water currents in taiwan strait. *Journal of Geophysical Research: Oceans*,  
872 122(6): 5005-5021.

873 Steiner, A. et al., 2017. Critical weather situations for renewable energies-part a: Cyclone  
874 detection for wind power. *Renewable Energy*, 101: 41-50.

875 Stommel, H., 2020. *The Gulf Stream*. University of California Press.

876 Thiebaut, S. and Vennell, R., 2010. Observation of a fast continental shelf wave generated  
877 by a storm impacting newfoundland using wavelet and cross-wavelet analyses.  
878 *Journal of Physical Oceanography*, 40(2): 417-428.

879 Thyng, K.M. et al., 2021. Performance of offline passive tracer advection in the regional  
880 ocean modeling system (roms; v3.6, revision 904). *Geoscientific Model  
881 Development*, 14(1): 391-407.

882 Toffoli, A., McConochie, J., Ghantous, M., Loffredo, L. and Babanin, A.V., 2012. The effect  
883 of wave-induced turbulence on the ocean mixed layer during tropical cyclones: Field  
884 observations on the australian north-west shelf. *Journal of Geophysical Research:  
885 Oceans*, 117(C11).

886 Umlauf, L. and Burchard, H., 2003. A generic length-scale equation for geophysical  
887 turbulence models. *Journal of Marine Research*, 61(2): 235-265.

888 Vincent, E.M. et al., 2012. Assessing the oceanic control on the amplitude of sea surface

889           cooling induced by tropical cyclones. *Journal of Geophysical Research: Oceans*,  
890           117(C5).

891 Warner, J.C., Defne, Z., Haas, K. and Arango, H.G., 2013. A wetting and drying scheme for  
892           roms. *Computers & Geosciences*, 58: 54-61.

893 Wu, R., Zhang, H. and Chen, D., 2020. Effect of typhoon kalmaegi (2014) on northern south  
894           china sea explored using multi-platform satellite and buoy observations data.  
895           *Progress in Oceanography*, 180: 102218.

896 Xu, J., Chao, S.-Y., Hood, R.R., Wang, H.V. and Boicourt, W.C., 2002. Assimilating high-  
897           resolution salinity data into a model of a partially mixed estuary. *Journal of*  
898           *Geophysical Research: Oceans*, 107(C7): 11-1-11-14.

899 Xu, Y. and Yu, X., 2021. Enhanced atmospheric wave boundary layer model for evaluation  
900           of wind stress over waters of finite depth. *Progress in Oceanography*, 198: 102664.

901 Yang, B., Hou, Y., Hu, P., Liu, Z. and Liu, Y., 2015. Shallow ocean response to tropical  
902           cyclones observed on the continental shelf of the northwestern south china sea.  
903           *Journal of Geophysical Research: Oceans*, 120(5): 3817-3836.

904 Zhai, X., Greatbatch, R.J., Eden, C. and Hibiya, T., 2009. On the loss of wind-induced near-  
905           inertial energy to turbulent mixing in the upper ocean. *Journal of Physical*  
906           *Oceanography*, 39(11): 3040-3045.

907 Zhang, F., Li, M. and Miles, T., 2018. Generation of near-inertial currents on the Mid-  
908           Atlantic Bight by Hurricane Arthur (2014). *Journal of Geophysical Research:*  
909           *Oceans*, 123(4): 3100-3116.

910 Zhang, H. et al., 2016. Upper ocean response to Typhoon Kalmaegi (2014). *Journal of*  
911           *Geophysical Research: Oceans*, 121(8): 6520-6535.

912